The geodynamic significance of UHP exhumation: New constraints from Tso Morari Complex, NW Himalaya

Anna K. Bidgood[1], Nick M W Roberts[2], Andrew J. Parsons[3], Dave Waters[1,4], Simon Tapster[2], Phillip Gopon[1]

[1] Department of Earth Sciences, University of Oxford, OX1 3AN, UK
[2] Geochronology and Tracers Facility, British Geological Survey, Nottingham, NG12 5GG, UK
[3]School of Geography, Earth and Environmental Sciences, University of Plymouth, PL4 8AA
[4] Museum of Natural History, University of Oxford, OX1 3PW, UK

AKB ORCID: 0000-0001-7750-9524
NMWR ORCID: 0000-0001-8272-5432
DJW ORCID: 0000-0001-9105-9953
AJP ORCID: 0000-0001-7538-9418
ST ORCID: 0000-0001-9049-0485
PG ORCHID: 0000-0003-3355-4416

*Correspondence (akbidgood@gmail.com)

Key Points

1. Geochronological constraints from the Tso Morari dome place the onset of exhumation from ultrahigh-pressure conditions at 46.91 ± 0.07 Ma
2. Close correspondence to other ultrahigh-pressure ages imply a similar time-frame for the onset of UHP exhumation across the NW Himalaya
3. The onset of UHP exhumation at 47-46 Ma coincides with significant geodynamic changes to local and wider plate network

Abstract

The burial and exhumation of continental crust to and from ultrahigh-pressure (UHP) is an important orogenic process, which is often interpreted with respect to the onset and/or driving forces of continent-continent collision. Here, we investigate the timing and significance of UHP metamorphism and exhumation of the Tso Morari complex, North-West Himalaya. We present new petrochronological analyses of mafic eclogites and their host-rock gneisses, combining U-Pb zircon, rutile and xenotime geochronology (high-precision CA-ID-TIMS and high-spatial resolution LA-ICP-MS), garnet element maps, and petrographic observations. Zircon from mafic eclogite have a CA-ID-

TIMS age of 46.91 ± 0.07 Ma, plus an LA-ICPMS age of 47.5 ± 0.8 Ma, with REE profiles indicative of growth at eclogite facies conditions. Those ages overlap with zircon rim ages (48.89 ± 1.1 Ma, LA-ICP-MS) and xenotime ages (48.1 ± 1.7 Ma; LA-ICP-MS) from the hosting Puga gneiss, which grew during breakdown of UHP garnet rims. We argue that peak zircon growth at 47-46 Ma corresponds to the onset of exhumation from UHP conditions. Subsequent exhumation through the rutile closure temperature, is constrained by new dates of 40.4 ± 1.7 Ma and 36.3 ± 3.8 (LA-ICP-MS). Overlapping ages from Kaghan imply a coeveal time-frame for the onset of UHP exhumation across the NW Himalaya, triggered by the arrival of buoyant Indian continental lithosphere into the Eurasian subduction zone. Our regional synthesis suggests that UHP exhumation at 46-47 Ma provides a time-stamp for major geodynamic shifts within the Himalayan orogen and the wider plate network, resulting from the India-Asia collision.

Key words: Radioisotope geochronology; mineral and crystal chemistry; petrography, microstructure and textures; Ultrahigh-pressure metamorphism; Continental margins: convergent

1. Introduction

The exhumation of continental crust from ultra-high pressure (*hereafter referred to as "UHP exhumation"*) is an important yet poorly constrained orogenic process (Guillot et al., 2009, Hacker and Gerya, 2013, Warren, 2013). Many studies relate UHP exhumation to other orogenic processes such as a reduction in the slab-pull force during the subduction of continental crust, slab break-off, and/or onset of various modes of orogenic extension/collapse (e.g., Brun and Faccenna, 2008, Yamato et al., 2008, Guillot et al., 2009, Hacker et al., 2010, Little et al., 2011, Burov et al., 2014, Chen et al., 2022). As such, UHP exhumation in the rock record is often interpreted to signify an important shift in the tectonic and geodynamic regime of an orogen (e.g., O'Brien et al. 2001; Yamato et al., 2008, Guillot et al., 2009, Hacker et al., 2010, Soret et al., 2021, Chen et al., 2022), for example, a shift from accretionary orogenesis to collisional orogenesis (c.f., Cawood et al., 2009). In an accretionary orogen, convergence is driven, and to some extent, accommodated by subduction of a trailing oceanic slab attached to the lower plate of the orogen. In contrast, in a collisional orogen, convergence is accommodated by crustal shortening and thickening, and may be driven by ongoing subduction elsewhere (e.g., Capitanio et al., 2015, Parsons et al., 2021, Bose et al., 2023). The transition between these regimes is likely to involve a change in slab-pull forces relating continental subduction and/or slab break-off, followed by UHP exhumation. Despite its importance as a marker of geodynamic change during orogenesis, the geodynamic processes responsible for UHP exhumation remain poorly constrained, and this prevents further understanding of its significance (Hacker and Gerya, 2013, Warren, 2013, O'Brien, 2019).

In order to understand the processes responsible for UHP exhumation, we must combine petrology-based pressure-temperature (P-T) pathways with geochronological constraints to determine the timing and rates of UHP exhumation through P-T space and with respect to the orogeny. However, attempts to constrain the timing and rates of UHP exhumation are always complicated by the uncertainty with which accessory phase ages are related to P-T paths (e.g. Kohn et al., 2017, O'Brien, 2019). This problem is clearly demonstrated in the UHP Tso Morari Complex of the NW Himalaya (Steck *et al.*, 1998; Epard and Steck, 2008; Guillot *et al.*, 2008).

The Tso Morari Complex is one of two UHP terranes in the NW Himalaya, the other being the Kaghan Valley Complex, located ~450 km to the west of Tso Morari (Steck *et al.*, 1998; O'Brien *et al.*, 2001; Parrish *et al.*, 2006; Epard and Steck, 2008; Guillot *et al.*, 2008; Buchs and Epard, 2019). Over the last three decades, geochronological studies of Tso Morari have yielded a range of estimates for the timing of UHP metamorphism and exhumation, spanning a period of 11 Ma (Leech, Singh and Jain, 2007; Donaldson *et al.*, 2013; St-Onge *et al.*, 2013). In contrast, estimates from the Kaghan UHP eclogites are tightly constrained to ~46 Ma (Kaneko *et al.*, 2003; Parrish *et al.*, 2006; Zhang et al 2022). From these constraints, a diverse but poorly constrained set of models have been proposed for the exhumation of Tso Morari and Kaghan Valley complexes (Schwartz *et al.*, 2007; Kylander-Clark et al., 2008; Möller *et al.*, 2015; Boutelier and Cruden, 2018).

The spread of ages for UHP metamorphism and exhumation in Tso Morari, could, to some extent, reflect differences in analytical techniques and their inaccuracies (e.g., Puetz and Spencer, 2023). However, a more likely cause is the difficulty and uncertainty associated with linking geochronological data with independently constrained metamorphic petrology (Foster and Parrish, 2006; Kohn et al., 2017, O'Brien, 2019). This problem is compounded further in the Tso Morari complex because UHP rocks exist as metre-scale eclogite facies mafic pods hosted within amphibolite facies felsic gneiss. Accessory phases suitable for geochronology are rare in eclogite pods, so some studies have attempted to relate the P-T evolution of eclogite pods with geochronological constraints from the amphibolite facies gneiss (St-Onge et al., 2013). However, this approach carries additional uncertainties surrounding the structural and metamorphic relationships between the eclogite pods and the amphibolite facies gneiss in which they are hosted (O'Brien, 2018).

To overcome these problems, estimates of the timing of UHP exhumation are better resolved using a combination of modern petrochronology techniques (Kohn et al., 2017), and where mineral size and zonation allows, high precision techniques (Parrish et al., 2006). The former can utilise a range of approaches, including: 1) the combination of geochronology, trace element geochemistry and metamorphic petrology, to quantitatively relate precise ages to specific stages on a metamorphic P-T path (e.g. Rubatto, 2002; Rubatto and Hermann, 2003); and 2) identifying and selecting a range of accessory phases associated with different metamorphic assemblages, which collectively span a wide range of closure temperatures (Regis et al., 2016; Lotout et al., 2018; Tual et al., 2022). Such techniques provide the best opportunity to accurately and precisely constrain the timing of UHP exhumation.

In this study, we employ a range of petrochronological techniques to precisely constrain the timing of UHP metamorphism and exhumation of the Tso Morari Complex. We use detailed petrographic analyses, including major and trace element x-ray maps of garnet, to identify and relate prograde, peak, and retrograde metamorphic assemblages in mafic eclogite samples and amphibolite facies felsic gneiss samples (the Puga gneiss). This allows us to select a variety of accessory phases from different metamorphic assemblages for U-Pb geochronology, to constrain the timing of metamorphism at different points of the P-T path. Using Laser Ablation Inductively Coupled Plasma Mass Spectrometry (LA-ICP-MS), we analyse zircon and rutile from an eclogite pod sample, and zircon, rutile, and xenotime from a felsic gneiss sample to constrain the timing of prograde, peak, and retrograde metamorphism. In addition, we analysed zircon from the eclogite using Chemical Abrasion Isotope Dilution Thermal Ion Mass Spectrometry (CA-ID-TIMS) to more precisely constrain the timing of zircon crystallization. Our results suggest that exhumation of the NW Himalaya from UHP conditions occurred synchronously across the Tso Morari complex and Kaghan Valley complex at ~47-46 Ma. We consider these results within the wider context of the Himalayan orogeny and discuss their implications for the physical processes and driving forces of UHP exhumation. Specifically, we interpret both the Kaghan and Tso Morari peak ages of ~47-46 Ma to correspond to the onset of UHP exhumation of Indian continental crust from the subducting Indian plate.

1.1 The Himalayan orogeny and the India-Asia collision: Definitions

In order to interpret our data with respect to the Himalayan orogeny and India-Asia collision, it is necessary to outline some definitions used hereafter. Tectonic models for the Himalayan orogeny and the India-Asia collision can be split into "Single Collision" and "Double Collision" models (e.g., Hu et al., 2016; Kapp and DeCelles, 2019, Parsons et al., 2020). Single Collision models propose a single continental collision between India and Eurasia, beginning at ~60 Ma and continuing to the present day (e.g., Gansser, 1966; Le Fort, 1975; Hu et al., 2016, Ingalls et al., 2016). Such models are not considered tenable as they require extreme volumes of continental subduction and cannot explain the significant kinematic and geodynamic changes which occur within the orogen and the surrounding plate network between 50-40 Ma (e.g., van Hinsbergen et al., 2019, Parsons et al., 2020, Parsons et al., 2021). As such, the results of this study are interpreted in the context of the competing "double collision" models, for which two alternative hypotheses exist, which differ with respect to the nature of the first collision. In these models, "first collision" began at ~60 Ma (e.g., Hu et al., 2015; An et al., 2021) but corresponds, to either (1) collision of the Indian continent with an equatorial Neotethys intra-oceanic arc (e.g., Patriat & Achache, 1984; Stampfli and Borel, 2004; Bouilhol et al., 2013; Replumaz et al 2014; Burg and Bouilhol, 2019); or (2) collision between an India-derived *microcontinent* and the Eurasian active margin (e.g., Sinha Roy, 1976; van Hinsbergen et al., 2019; Zhou and Su, 2019).

"Second collision" occurred between the Indian continent and the Eurasian active margin sometime between 50 Ma to 25 Ma (e.g., Patriat & Achache, 1984; Replumaz et al 2014; Burg and Bouilhol, 2019, Searle, 2019, van Hinsbergen et al., 2019, Parsons et al., 2021). In the context of these double collision models, the Himalayan orogeny corresponds to collisional deformation of Indian continental rock which initiated during first collision and continued through second collision. In contrast, the "India-Asia collision" *sensu-stricto* corresponds to the second collision event only (e.g., Parsons et al., 2020). Debate continues to surround the relative validity of the two "double collision" hypotheses and further considerations can be found in recent reviews (e.g., Kapp and DeCelles, 2019, Searle, 2019, van Hinsbergen et al., 2019, Parsons et al., 2020); our study is presented in the context of both double collision models (e.g., Burg & Bouihol 2019 versus van Hinsbergen et al. 2019) as it is beyond the scope of the new data presented in this paper to address their relative validity.

1.2 Geology of the Tso Morari Complex

The Tso Morari dome is situated on the north-western margin of the Indian plate (Figure 1), and is separated from the Ladakh batholith of the Asian plate located to the north by the Indus suture zone (Fuchs and Linner, 1996). The Tso Morari dome comprises a set of stacked nappes, folded into a northwest-southeast trending periclinal antiform. (Steck *et al.*, 1998; Buchs and Epard, 2019). The structurally lowermost nappe is the Tso Morari Complex (also known as the Tso Morari Gneiss, Epard & Steck, 2008), which crops out in the centre of the dome. The Tso Morari Complex contains Ordovician granite and disrupted mafic dykes and sills intruded into Cambrian sediments of the Indian continent. Granitic rocks are variably deformed, resulting in an array of undeformed metagranites, augen gneiss and garnet-mica-schists within the Tso Morari Complex. The range of deformation states preserves different parts of the P-T-t history of the Tso Morari Complex. The early subduction-related history is rarely preserved except as thin corona textures in low strain metagranite (Bidgood et al, 2022), whereas the high strain gneisses are often overprinted by later, amphibolite facies metamorphism and exhumation-related deformation. These end-member states are distinguished locally as the Polokongka La granite and the Puga Gneiss, which share the same granitic protolith, and differ only in their state of strain and metamorphic evolution (Girard and Bussy, 1999).

Mafic rocks within the Tso Morari complex locally preserve eclogite-facies mineral assemblages formed at conditions of > 26 kbar, 500-645°C (e.g. de Sigoyer and Guillot, 1997; Guillot et al., 1997; St-Onge *et al.*, 2013; Bidgood *et al.*, 2020). Evidence of high-pressure metamorphism is rarely observed in the felsic metagranitoid rocks but has been recorded by glaucophane-bearing metasediments (Guillot et al., 1997), pseudomorphs after coesite within the Polokongka La granite (Bidgood *et al.*, 2020) and thin corona textures and pseudomorphs after cordierite in low strain metagranites (Bidgood et al, 2022). Later overprinting at amphibolite-facies conditions is recorded in the retrogressed mafic eclogites at 610 ± 30°C at 9 ± 3 kbar (de Sigoyer et al., 1997) and in the felsic rocks at 650 ± 50°C at 9 ± 1 kbar (Girard, 2001), 630°C ± 30°C at 9 ± 2 kbar (Guillot et al., 1997) and 725 ± 50°C at 7.1 ± 1 kbar (St-Onge et al., 2013).

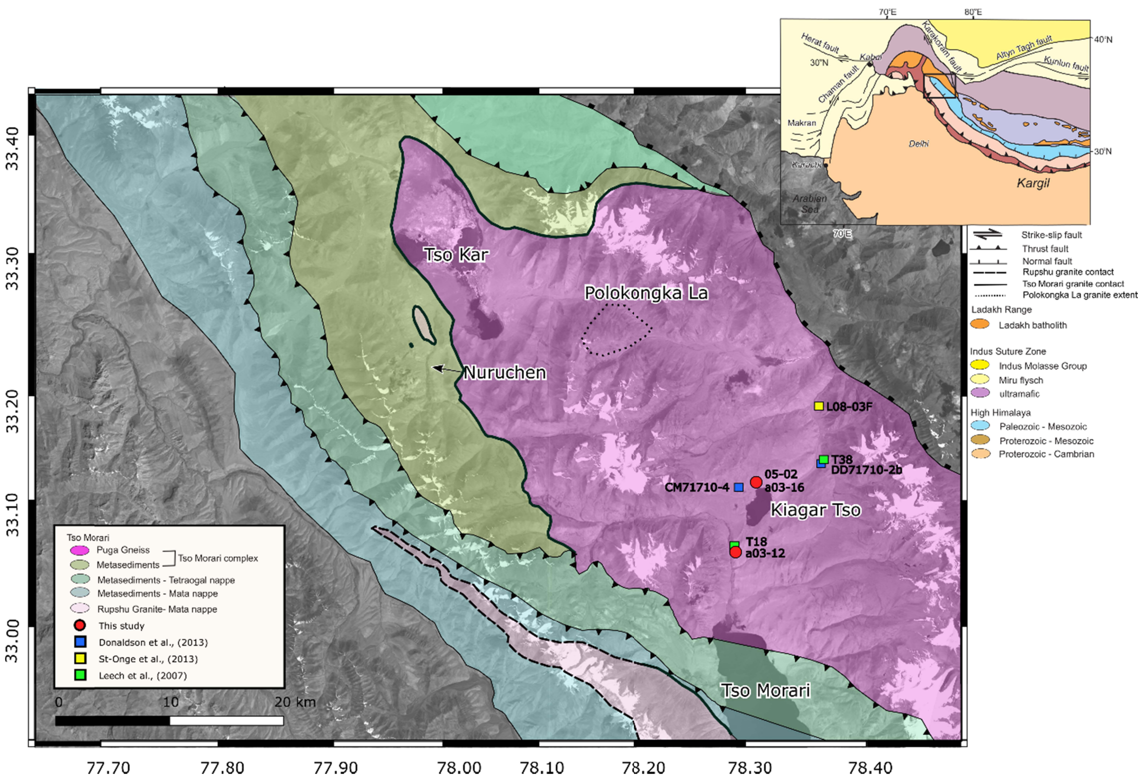

Figure 1. Geological map adapted from Epard and Steck (2008), St-Onge et al. (2013) and references therein, showing location of geochronological samples. Background USGS landsat data downloaded from https://earthexplorer.usgs.gov/. Colouring corresponds to bands 762, greyscale by luminosity.

1.3 Geochronology of the Tso Morari Complex

The Puga Gneiss and Polokongka La granite contain zircon with thin metamorphic rims surrounding igneous cores, with the latter dated by U-Pb at 479 ± 1 Ma (Girard and Bussy, 1999; Leech et al., 2007). Initial estimates of the age of high pressure metamorphism by De Sigoyer et al. (2000) used Lu-Hf isochron ages on garnet-clinopyroxene-whole-rock data, Sm-Nd on garnet-glaucophane-whole-rock data, and U-Pb in allanite, giving ages of 45 ± 4.4 Ma, 55 ± 12 Ma and 55 ± 17 Ma, respectively. These estimates attempted to date minerals which can definitively be linked to metamorphic reactions/conditions, although this was hindered by the large uncertainties on these dates.

Four clusters of zircon growth were recorded in the Puga Gneiss by Leech et al (2007) by U-Pb LA-ICP-MS dating of the metamorphic rims found around igneous zircon grains (n = 19), and are interpreted to represent ultrahigh-pressure metamorphism at 53.3 ± 0.7 Ma, followed by further zircon growth in eclogite facies conditions and an amphibolite facies overprint at 45.2 ± 0.7 Ma. St-Onge et al. (2013) recorded monazite and allanite U-Pb SHRIMP ages of 45.3 ± 1.1 Ma and 43.3 ± 1.1 Ma respectively, interpreted to represent post-eclogite facies peak temperature metamorphism of 7–8.4 kbar at 705–755 °C, based on pseudosection modelling of the observed garnet breakdown reaction. Cooling through phengite, biotite and muscovite Ar-Ar closure temperatures is recorded at 48 ± 2 Ma, 31.1 ± 0.3 and 29.3 ± 0.3 Ma (De Sigoyer et al., 2000) respectively, with further cooling recorded by apatite and zircon fission track data at ~23.5 – 7.5 Ma (Schlup et al., 2003). Dates from within the Puga Gneiss are dominated by post-peak, amphibolite facies ages recording Barrovian metamorphism, cooling and uplift.

The mafic eclogites better preserve the early high-pressure metamorphic history in their major and accessory mineral assemblages. St-Onge et al (2013) analysed zircon in situ with SHRIMP U-Pb geochronology, yielding an age of 58.0 ± 2.2 Ma (n = 2) for zircon included in the core of a garnet, and 50.8 ± 1 Ma (n = 4) for zircon included/adjacent to matrix barroisite, phengite and garnet. The older age is interpreted to record zircon crystallisation during prograde garnet growth to high pressure, and the younger age is interpreted to represent peak metamorphism in the eclogite facies. Donaldson et al. (2013) used split-stream LA-ICP-MS to measure the U-(Th)-Pb and REE abundances of in situ zircon from two mafic eclogites, located ~10 km apart. Lower intercept dates of each sample overlap at 45.3 ± 1.6 Ma and 44.2 ± 1.2 Ma; however, the authors interpret the spread in common-lead corrected ages (ca. 53 to 37 Ma), with a peak at 47 – 43 Ma and consistent REE signatures (absence of Eu anomaly and flat HREE), as reflecting protracted zircon crystallisation in the eclogite facies.

The age of UHP metamorphism in the Kaghan Valley Complex has been estimated using U-Pb SHRIMP and U-Pb ID-TIMS analyses of zircon from eclogite-facies mafic rocks, yielding ages of 46.2 ± 0.7 Ma (Kaneko et al., 2003) and 46.4 ± 0.1 Ma (Parrish et al., 2006), respectively. These zircons were found included in UHP garnet rims with coesite inclusions. Eclogite facies ages of zircon and allanite from Kaghan were also estimated using U-Pb and Th-Pb ID-TIMS analyses at 45.5 ± 6.6 Ma and 46.5 ± 1.0 Ma, respectively (Parrish et al., 2006). An additional age of eclogite facies zircon was estimated using U-Pb SIMS at 46 ± 2 Ma in Naran, 30 km south-west of Kaghan (Zhang et al., 2022). A compilation of geochronology of high pressure metamorphism in the north west Himalaya can be found in Supporting Information 1.

Given the differences in analytical techniques used to date the Tso Morari complex and the difficulty in relating these dates to metamorphic stages, it remains unclear to what degree the spread of ages from Tso Morari can be assigned to geological heterogeneity or to analytical uncertainty and artifacts. For example, the absence of petrographic context in some studies makes it difficult to interpret the age clusters with respect to specific metamorphic conditions (see O'Brien, 2006 for further discussion). Additionally, given the types of analyses used in Tso Morari, it is not possible to tell if zircon growth in the mafic eclogites was prolonged, or if the data represent mixed ages; this is hampered the presence of common lead in the present data. The outcome of these two hypotheses has significant implications for the process of continental subduction and UHP exhumation, particularly in light of the narrow age spread for UHP metamorphism from Kaghan only 450 km away. It is not clear whether the differences between Tso Morari and Kaghan reflect analytical biases or inaccuracies, or a complex process of continental subduction and exhumation such as diachronous and/or prolonged burial and exhumation.

2. Petrography

2.1. Analytical methods

Petrographic study of 29 mafic eclogites and 28 Puga Gneiss samples from the Tso Morari Complex was undertaken, with one fresh eclogite (a03-16), one retrogressed eclogite (a03-12) and one gneiss sample (05-02) selected for further analysis. Major element compositions of minerals that exhibit solid solutions were measured using a Cameca SX-5 field emission electron microprobe at the University of Oxford, with a 15 keV acceleration potential, 20 nA beam current, 30 second count time per major element (30 second background) and 60 second count time on Ti (60 second background). A range of natural and synthetic oxide standards were used including albite (Na, Al, Si), Orthoclase (K), MgO (Mg), wollastonite (Ca), andradite (Fe), Mn metal (Mn) and synthetic TiO2 (Ti) and analyses were verified against secondary mineral standards. Mineral spot analyses and line profiles were taken across garnet to determine the extent of intracrystalline compositional variation (see Supporting Information 2).

Quantitative major element X-ray maps were collected from polished thin sections using the CAMECA SX-5 field emission electron microprobe at the University of Oxford at a working distance of 10 mm, a 15 keV acceleration potential, 170 nA current, 0.06 s dwell time and a 3 μm step size for the elements P, Ca, Mn, Mg and Fe. A dwell time of 0.032 s and a 200 nA beam current were used for the elements Al, Si, Ti, Y and Yb. A range of natural and synthetic oxide standards were used including Durango apatite (P), andradite (Ca, Fe), Mn metal (Mn), MgO (Mg), albite (Al, Si), TiO2 (Ti), Y metal (Y), Yb metal (Yb).

2.2. Petrography and petrology: Observations

2.2.1. Puga Gneiss (sample 05-02): petrography

Puga Gneiss sample 05-02 was collected from the north shore of Kiagar Tso (33.1214°N, 78.2958°E), the middle of the Tso Morari Complex. Sample 05-02 is a strongly-foliated, garnet-bearing gneiss comprising albite, quartz, muscovite, biotite and garnet, with accessory zircon, apatite, rutile, and xenotime.

Sample 05-02 is dominated by a schistosity (S2) defined by bands of white mica, albite and quartz (Figure 2a) which wrap around larger garnet porphyroclasts. Quartz occurs in polycrystalline ribbons or lenses separated by narrow bands of white mica, indicative of a high-strain fabric (Figure 2a-d). The quartz ribbons are cut by discontinuous shear bands forming an S-C′ fabric. Quartz grains are > 200 μm and equant with amoeboid shapes along grain boundaries associated with dynamic recrystallization in the grain boundary migration (GBM) regime (Stipp *et al.*, 2002). Albite bands and lenses are largely composed of fine-grained aggregates. Among these, larger feldspar grains show subgrains of similar size to the dominant population, suggesting that dynamic recrystallization occurred in the subgrain rotation (SGR) regime for feldspar (Passchier & Trouw, 2005). Zircon and rutile occur in the matrix.

Garnet porphyroblasts of varying size and abundantly fractured, are scattered through the rock. They are partly replaced by biotite, white mica and chlorite. The studied section contains one large (6 x 5 mm) ovoid garnet porphyroblast (Figure 3) that contains significant detail (see below). Fine-grained inclusion trails of quartz and rutile within garnet define a primary foliation (S1), which is oblique to the matrix fabric (S2) and folded at the core-rim boundary (Figure 3a). Kyanite is observed within the garnet core, adjacent to a staurolite grain, surrounded by white mica. The garnet has a corroded grain shape in which embayments contain biotite, white mica and xenotime.

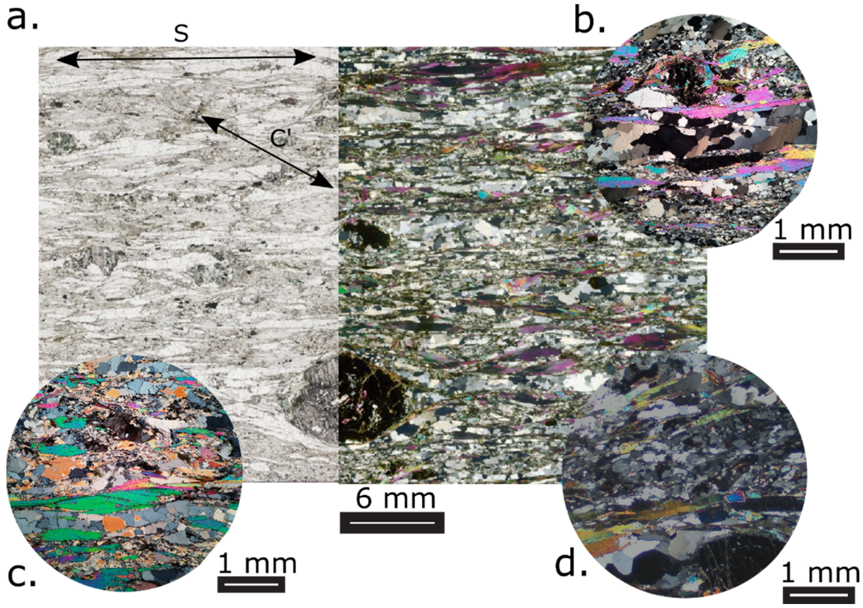

Figure 2. a. Puga Gneiss Sample 05-02. PPL and XPL image showing gneissose texture consisting of quartz-rich, feldspar-rich and mica-rich layers. Large garnet wrapped by fabric (S2) shown in Figure 3. b-c Puga Gneiss Sample 05-01, adjacent to 05-02. b. Polycrystalline quartz-rich band in between mica sheets. Recrystallised quartz shows undulose extinction. Quartz grains in the lower part of the image span the width of the mica ribbons. c. Stacked white mica sheets curve into high strain fabric showing top to the right sense of shear. Annealed quartz band and dusty albite and apatite present. d. Puga Gneiss Sample 05-02. Fine-grained albite lens between mica sheets.

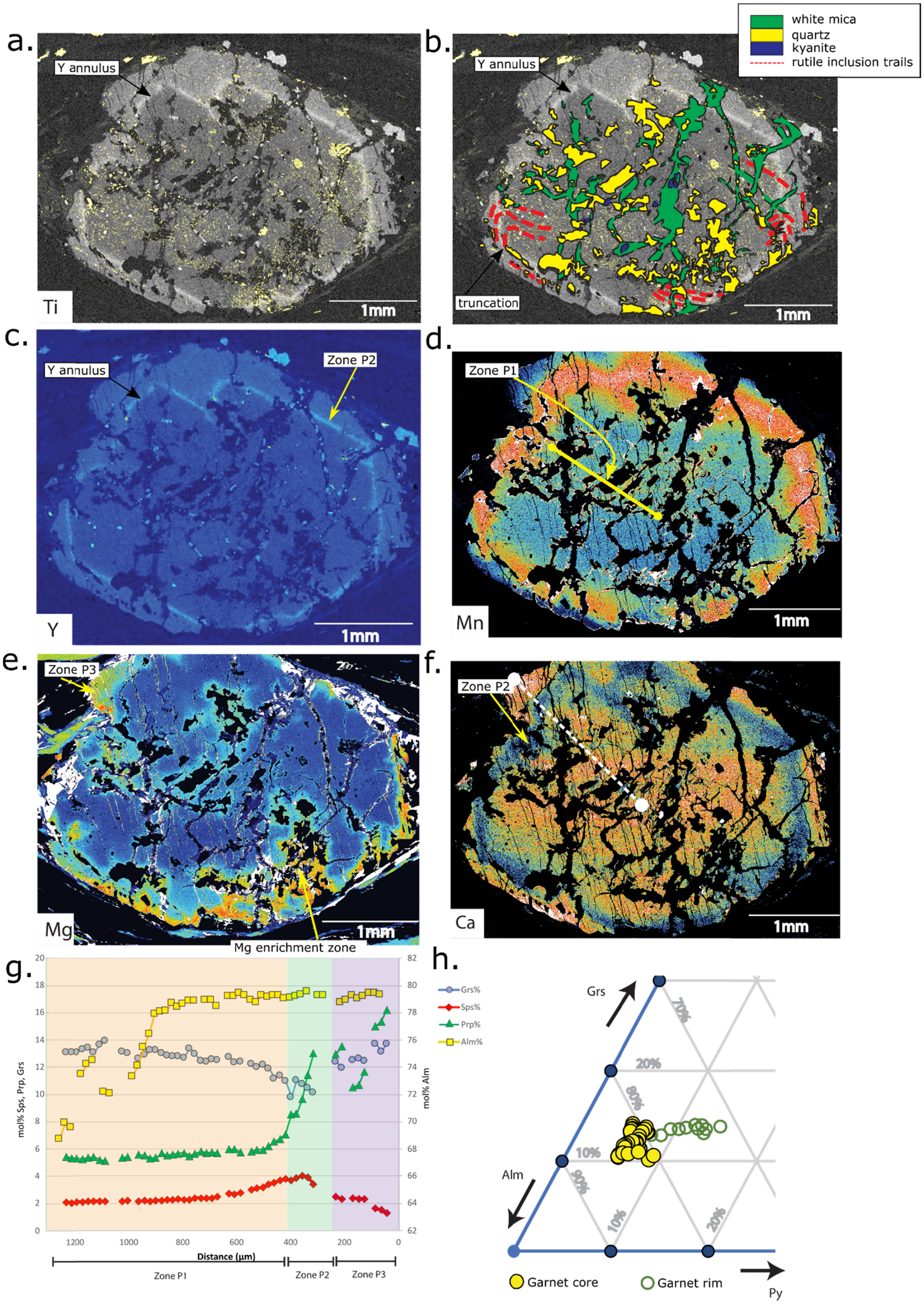

Figure 3. Puga Gneiss Sample 05-02 garnet. **a**. Ti map (yellow) overlying Y map, showing orientation of rutile inclusions and location of rectangular rutile clusters. **b**. Inclusion map of garnet. Location of the core-rim boundary defined by the yttrium high. **c-f.** Yttrium, manganese, magnesium

and calcium EPMA element maps. **g.** Garnet zoning profiles from core (left) to rim (right).**h.** Ternary diagram of transect across garnets. Approximate location of garnet transect shown by white dashed line on insert f.

2.2.2. Puga Gneiss (sample 05-02): garnet composition

Major and trace element maps of the large garnet exhibit concentric zonation, comprising three distinct zones (Figure 3). The garnet core (zone P1) has an approximately constant composition of $Alm_{79}Grs_{12.5}Pyr_{5.5}Spss_{4\text{-}2.3}$ and a faceted garnet shape, outlined by a manganese- and yttrium-rich annulus. Inclusions of quartz, rutile and white mica are found throughout zone 1, whereas inclusions of kyanite are restricted to the inner portion of zone P1. Zone P2 surrounds the zone 1 core and is defined by a calcium trough (10% Grs) and manganese-high with a faceted outline. Zone P3 defines a magnesium- and calcium-high, manganese-low rim, which shows an increase in pyrope (to 16%) and grossular (to 13%) with a decrease in almandine (to 69%). Zones P2 and P3 contain quartz, white mica, and rutile inclusions, but to a lesser extent than in zone 1. Kyanite is absent from zones P2 and P3. In zones P1 and P2, magnesium-enriched haloes are developed along the internal fracture network, surrounding many larger inclusions of white mica and quartz, and connecting with the outer zone of the garnet.

2.2.3. Mafic eclogite (sample a03-16): petrography

Sample a03-16 is a mafic eclogite taken from the same locality as Puga Gneiss sample 05-02 (33.1214°N, 78.2958°E), adjacent to sample CM71710-4 of Donaldson et al. (2013), and displays similar features to mafic eclogites described from other localities in the Tso Morari Complex (e.g. Jonnalagadda et al., 2017; O'Brien & Sachan, 2000; Palin et al., 2014; St-Onge et al., 2013; Wilke et al., 2015). Sample a03-16 has a medium- to coarse-grained granoblastic texture with a major mineral assemblage of garnet, omphacite, phengite, quartz, and talc, with minor amounts of clinozoisite, amphibole, carbonate, rutile and zircon.

Garnet and omphacite (Figure 4a) are in textural equilibrium, forming straight-edge contacts, with coarse grained homogeneous phengite and talc. In some places, symplectites after omphacite are observed, comprised of amphibole, plagioclase and occasional diopside. Dolomite is also present in the matrix as large poikiloblasts containing inclusions of phengite, omphacite and rutile.

Compositionally zoned amphiboles exist in the matrix and as inclusions in garnet (Figure 4b). Amphibole inclusions are zoned blue-green and generally darker in colour than that in the matrix, whereas matrix amphiboles are blue-green to pale green and coarse-grained. Thin mantles of pale green amphibole surround garnet and fine-grained intergrowths of biotite and plagioclase surround phengite. Matrix quartz and omphacite contain clusters of zircon inclusions, whereas garnet, omphacite, quartz, phengite, and talc contain rutile inclusions (Figure 4c). Garnet occurs as subhedral porphyroblasts that are 3-4 mm in diameter (Figure 4b) and contain inclusions of zoned blue-green amphibole, and also quartz and rutile. Rutile commonly forms angular clusters of grains, both in the matrix and within garnets, which we interpret as replacing a former igneous Fe-Ti oxide.

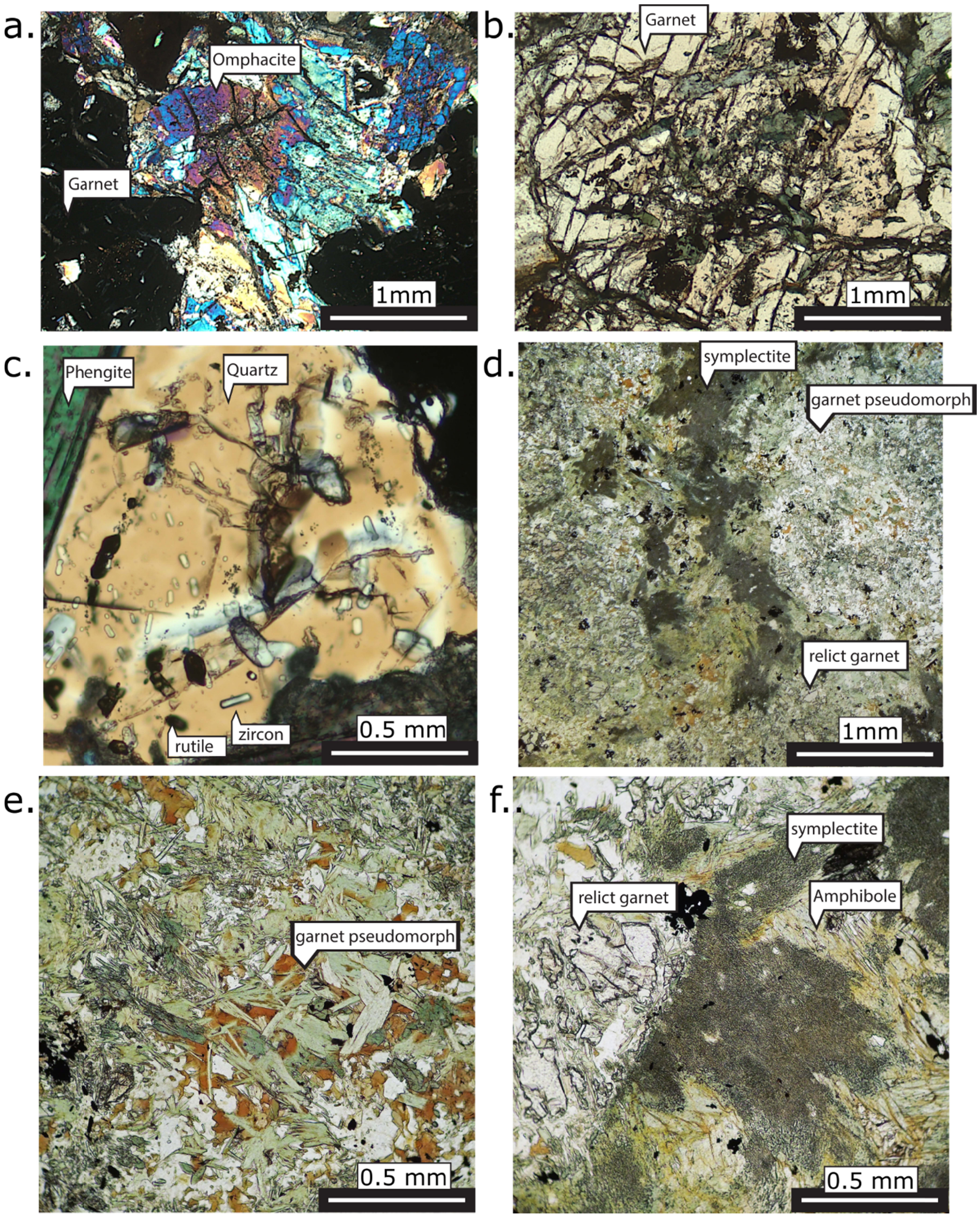

Figure 4. Photomicrographs of mafic eclogites. A. Sample a03-16, XPL, poikiloblastic garnets and omphacite. B. Sample a03-16, colour zoning in garnet with amphibole inclusions ranging in colour from blue to green. C. Sample a03-16, matrix quartz with abundant high relief zircon and dark rutile

inclusions. D-f. Sample a03-12 retrogressed mafic eclogite. D. Subhedral pseudomorphed garnets present on the edge of the image. Dark-coloured, fine-grained intergrowth of plagioclase and amphibole (symplectite) after omphacite. Coarse-grained, green matrix amphiboles interlocked with omphacite pseudomorphs. E. Core of large pseudomorphed garnet showing aggregate of chlorite, biotite and minor green amphibole set in plagioclase. F. Dark amphibole-plagioclase symplectite after omphacite adjacent to partly pseudomorphed garnet.

2.2.4. Mafic eclogite (sample a03-16): garnet composition

Major and trace element maps of a single garnet in sample a03-16 show three zones. Zone E1 defines the core region, which has a composition of $Alm_{48\text{-}42}$ $Grs_{24\text{-}29}$ $Pyr_{20\text{-}30}$ $Sps_{6\text{-}1}$, with increasing almandine and pyrope components from core to rim (Figure 5 b and c). The rim of the zone E1 core is outlined by a manganese-high annulus. Zone E2 surrounds the zone E1 core and is defined by a calcium trough with a faceted outline (Figure 5 d and e). Zone E3 forms along the garnet rim defined by a magnesium-high, manganese-low rim with shows an increase in pyrope (to 30-35%) and grossular (to 30%, decreasing to 16% at the outer rim). Magnesium-enriched E3-like domains also extend in some places from the outer rim towards the core of the garnet, cutting across concentric garnet zones E1 and E2, and surrounding inclusions, often forming channelized features (Figure 5 b and c).

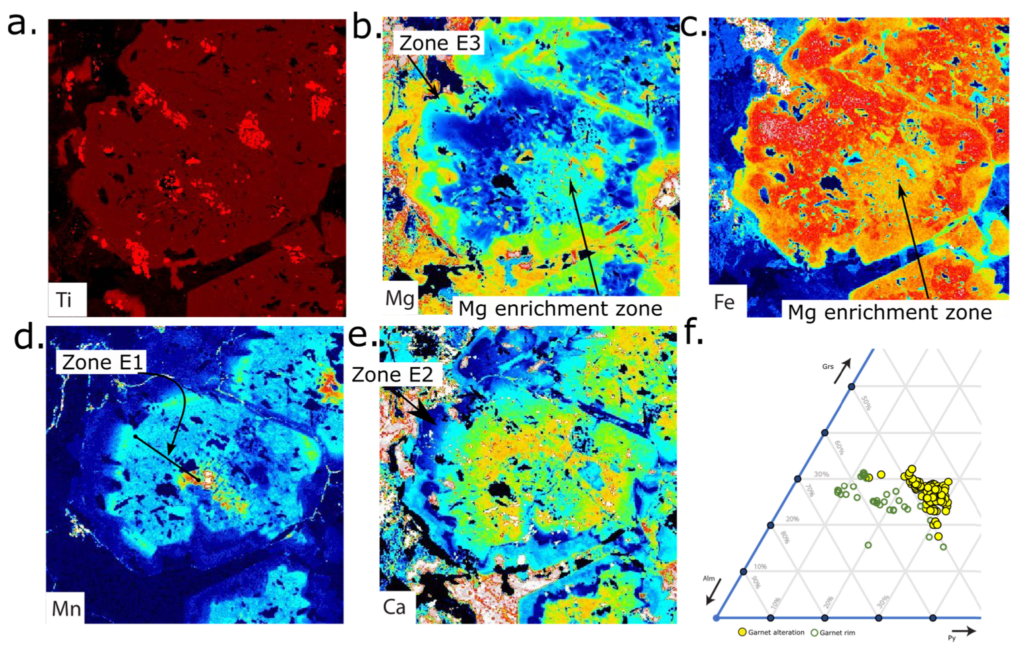

Figure 5. Garnet maps from mafic eclogite sample a03-16. A. Ti map showing clusters of rutile inclusions forming distinct shapes after Fe-Ti oxides. B-e. Mg, Fe, Mn and Ca maps showing concentric zoning patterns cut by Mg-Fe embayments emanating from the outside rim of the garnet. F. Ternary diagram of transect across garnet showing Fe-Mg alteration and garnet rim.

2.2.5. Retrogressed mafic eclogite (sample a03-12): petrography

Sample a03-12, along with the adjacent sample a03-09, is a retrogressed mafic eclogite from 'The Bridge' locality (33.0677°N, 78.2758°E), ~8 km south of sample a03-16. This is the same locality sampled and analysed by Leech et al. (2007) (their sample T18). The samples are composed of garnet, amphibole, plagioclase, biotite, chlorite, ilmenite, rutile and zircon. Relict garnet is preserved within pseudomorphs that preserve subhedral garnet shapes, but are largely replaced by plagioclase, hornblende, biotite and chlorite aggregates (Figure 4 d and e). Matrix omphacite has been pseudomorphed by fine-grained amphibole and plagioclase intergrowths (Figure 4f). Zoned, blue-green matrix amphibole retains the habit and textural association of the post-peak, pre-feldspar-stability sodic-calcic amphiboles (cf. Palin *et al.,* 2014). Chlorite and biotite form aggregates which overprint the surrounding metamorphic patterns. Rutile grains occur in garnet and matrix amphibole, and are rimmed or replaced by ilmenite in retrogressed areas. Zircon is distributed in small grains in the matrix.

2.3.Petrography and petrology: Interpretation and metamorphic correlation

2.3.1. Puga Gneiss (sample 05-02)

The Puga Gneiss (sample 05-02) displays evidence of two metamorphic assemblages. The first is defined by the garnet compositional zoning from P1 to P3, and the inclusion suite of quartz, kyanite, rutile and zircon. Quartz and rutile inclusions define a crenulated primary foliation (S1), and kyanite is found exclusively within garnet. The garnet compositional zoning is consistent with prograde growth culminating in eclogite-facies conditions. The magnesium distribution in the garnet interior implies that some fracturing occurred at near-peak conditions.

The second assemblage is defined by the rock matrix grains outside the garnet porphyroblasts, which form a segregated quartz-feldspar-mica mineral banding modified by an S-C′ fabric. Accessory minerals in this matrix assemblage include rutile and zircon. Dynamic recrystallization of quartz in the GBM regime implies a deformation temperature in excess of 530°C (Stipp et al., 2002), and evidence for subgrain rotation in albite is consistent with about 600°C (Passchier & Trouw, 2005). No lower-temperature dynamic recrystallization microstructures are observed, and minor chlorite, generally associated with garnet, is undeformed. Rutile is stable in the rock matrix, commonly enclosed in white mica. Based on these observations, we interpret the matrix assemblage to reflect metamorphism and deformation on the retrograde path, at amphibolite-facies conditions.

A distinct mineral association surrounds the large garnet, where xenotime grains are hosted in micaceous aggregates that form in embayments where the Mg-rich rim zone (P3) of the garnet is missing, due to partial resorption of garnet. We infer that the xenotime is formed from yttrium liberated by garnet breakdown after peak eclogite-facies conditions were achieved.

2.3.2. Mafic eclogite (sample a03-16)

Sample a03-16 contains three identifiable metamorphic assemblages. Garnet and omphacite (Figure 4a) in textural equilibrium with coarse grained homogeneous phengite and talc define a peak pressure eclogite-facies mineral assemblage (e.g., M2 of St-Onge et al., 2013). Accessory phases within this peak assemblage include zircon, present as clusters of grains included within matrix quartz and omphacite, and rutile, present as inclusions, commonly clustered, within garnet, omphacite, quartz, phengite, and talc (Figure 4c). Initial growth of these zircon and rutile grains may have begun prior to eclogite facies metamorphism. Within garnet, the increase in pyrope component from core to rim, displayed by zones E1 to E3, corresponds to garnet growth during prograde to peak eclogite conditions. We interpret zones E1 to E3 as a prograde to peak assemblage, where zone E3 correlates with the omphacite, phengite and talc peak assemblage described above.

The second metamorphic assemblage is defined by the early breakdown products of the peak assemblage phases. The dominant example is the zoned blue-green matrix amphibole, which may represent the product of talc dehydration as well as the influx of external fluids under eclogite-facies conditions (cf. Palin et al., 2014).

The third assemblage includes feldspar-bearing symplectites after omphacite, and secondary fine-grained white mica aggregates forming in the irregular rims of coarse-grained phengite. These represent an amphibolite-facies overprint.

2.3.3. Retrogressed mafic eclogite (sample a03-12)

Sample a03-12 is dominated by a post-peak metamorphic assemblage, whereas the peak assemblage displayed by sample a03-16, is identifiable in a03-12 as relict garnet grains and pseudomorphs after garnet and omphacite. Blue-green amphiboles are interpreted as an early post-peak phase, which grew within the eclogite facies field prior to the appearance of stable sodic feldspar during decompression (e.g., Palin et al., 2014). The rest of the post-peak assemblage is typical of an amphibolite facies retrograde assemblage characterised by fine-grained amphibole and plagioclase intergrowths. Aggregates of chlorite and biotite characterise a lower amphibolite facies overprint. Rutile is found within prograde relict garnets as well as the matrix and has no indication of internal zonation. We therefore interpret rutile as a relict grains from a prograde or peak assemblage, rather than a new phase that nucleated during latest-stage lower amphibolite facies metamorphism. Zircon is present throughout this sample, predominantly as inclusions in peak omphacite and quartz, suggesting that it crystallised prior to omphacite breakdown in the eclogite facies.

2.3.4. Correlation of metamorphic assemblages (M1, M2, M3) in the Puga Gneiss and mafic eclogites

Comparison and correlation of the petrography and petrology of samples 05-02, a03-16, and a03-12, allows for the definition of three distinct metamorphic assemblages that reflect distinct portions of the same P-T path of the Tso Morari complex, experienced and recorded by both lithologies. Crucially, these assemblages provide a robust means for linking accessory phase geochronology to metamorphic evolution of the Tso Morari complex. These metamorphic assemblages and their constituent accessory phases are summarised as follows:

2.3.4.1. M1: Prograde-to-peak eclogite facies assemblage

Zones P1 and P2 of garnet within the Puga gneiss sample 05-02 and zone E1 and E2 of garnet in the mafic eclogite a03-16 define the M1 prograde-to-peak, eclogite facies assemblage. This includes inclusions of kyanite, quartz, white mica, zircon and rutile, within garnet in 05-02.

2.3.4.2. M2: Peak eclogite facies assemblage

High-Mg rims of garnet, plus omphacite, phengite, quartz and talc in mafic eclogite sample a03-16 define the M2 peak eclogite facies assemblage. M2 also includes the high-Mg garnet rims in Puga gneiss sample 05-02. Elsewhere in Tso Morari, similar garnet rim compositions in mafic eclogites contain inclusions of coesite or polycrystalline inclusions after coesite (Sachan *et al.*, 2004). Remnants of this assemblage are also preserved by relict garnet in the retrogressed mafic eclogite sample a03-12.

2.3.4.3. M3a/M3b/M3c: Post-peak assemblage

The M3 post-peak assemblage reflects continuing metamorphism from eclogite to lower amphibolite facies conditions, and is subdivided to reflect this. In the mafic eclogite samples (a03-16, a03-12), M3a is recorded by growth of coarse-grained blue-green amphiboles in the eclogite facies, which elsewhere in the Tso Morari Complex, has been linked to the breakdown of talc and the influx of fluid at 23 and 19 kbar respectively (Palin et al., 2014). Post-peak assemblage M3b corresponds to upper amphibolite facies retrograde metamorphism. In the mafic eclogite samples (a03-16, a03-12) M3b is defined by symplectites of fine-grained amphibole and plagioclase intergrowths after omphacite. The lower-temperature association of chlorite with biotite, largely as a replacement of garnet cores in a03-12, can be assigned to M3c.

In Puga gneiss sample 05-02, initial garnet breakdown and the associated nucleation of xenotime, occurred at eclogite to upper amphibolite facies, and therefore correlates with either the M3a or M3b post-peak assemblages observed in the mafic eclogites. M3b is defined by the matrix assemblage of quartz + albite + muscovite, which also contains zircon and rutile, and displays quartz microstructures indicating post-peak deformation temperatures of >530 °C. M3c corresponds to lower amphibolite facies retrograde metamorphism and is represented by overprinting aggregates of chlorite and biotite after garnet.

3. U-Pb Geochronology

3.1. Analytical methods

Zircon grains from the heavy, non-magnetic fraction of sample a03-12 were imaged via cathodoluminescence (CL) using an FEI Quanta 650 environmental scanning electron microscope (E-SEM) at the University of Oxford, using a 10 kV electron beam, 16mm working distance and a beam current of 0.49nA. Zircon grains from sample 05-02 were also mounted on sticky tape in order to analyse the <10 μm thick rims. Rutile grains chosen for analysis were picked from the non-magnetic fraction and were imaged via backscatter electron imaging (using the same E-SEM) to determine the homogeneity of the grains chosen for analysis. None of the rutile grains showed any evidence of zoning. Xenotime was measured in a polished thin section in order to preserve the petrographic relationships observed.

All geochronology and mineral separation were conducted at the Geochronology and Tracers Facility, British Geological Survey, Nottingham, UK. Laser ablation inductively-coupled plasma mass spectrometry (LA-ICP-MS) was conducted using a Nu Instruments AttoM sector-field single-collector ICP-MS, coupled to an Elemental Scientific Lasers 193nm UC Excimer laser ablation system fitted with a TV2 cell. The method follows that described in Roberts et al. (2016), with uncertainty propagation following recommendations of Horstwood *et al.* (2016), and age calculation and plotting using IsoplotR (Vermeesch, 2018). Common lead corrected ages, where quoted, use a ^{207}Pb-based method (Chew et al., 2014) and assume a Stacey and Kramers (1975) initial lead composition, and concordance of the final age. All uncertainties are quoted and plotted at 2σ. Trace elements were measured using the same instrumentation as for U-Th-Pb, with the Attom measuring in linkscan mode (see Supporting Information 3 for full analytical protocol), with normalisation to GJ-1 zircon (Piazolo *et al.*, 2017).

Zircon in one sample (a03-12) was further analysed by Chemical Abrasion Isotope Dilution Thermal Ionisation Mass Spectrometry (CA-ID-TIMS), following analytical and data reduction methods described by Tapster *et al.* (2016), and utilising the ET535 EARTHTIME mixed tracer (Condon *et al.*, 2015).

3.2. Puga Gneiss (sample 05-02)

3.2.1. Zircon

Zircon grains in the Puga gneiss sample 05-02 show oscillatory zoning and a euhedral shape, indicative of igneous zircon, with a Th/U of 0.05 – 0.26. Thin, bright rims (< 20 µm) are present surrounding the dark cores. From the epoxy mounted zircon, 33 LA-ICP-MS analyses of zircon cores were obtained from 21 grains. Five ages ranging from 1020 Ma to 2481 Ma ($^{207}Pb/^{206}Pb$ age), indicate a population of xenocrystic zircon inherited during emplacement of the Puga gneiss igneous protolith. Nine analyses had ages that were discordant by >10 %, and were discarded from age calculation. Of the remaining 19 concordant analyses, 17 spots provide a concordia age of 482.0 ± 3.33 Ma with a mean square of weighted deviates (MSWD) value of 1.5 (Figure 6a). Using spot analysis of tape-mounted zircon, whereby the outer rim can be targeted more confidently, 64 grains yielded a spread of ages from ca. 48 Ma to 569 Ma (Figure 6b). A broad plateau of ages overlaps the mounted zircon at ca. 480 Ma, consistent with our weighted mean concordia age. The youngest three analyses provide a weighted mean, using common lead corrected $^{206}Pb/^{238}U$ ages, of 48.89 ± 1.12 Ma (MSWD = 1.3; Figure 6b).

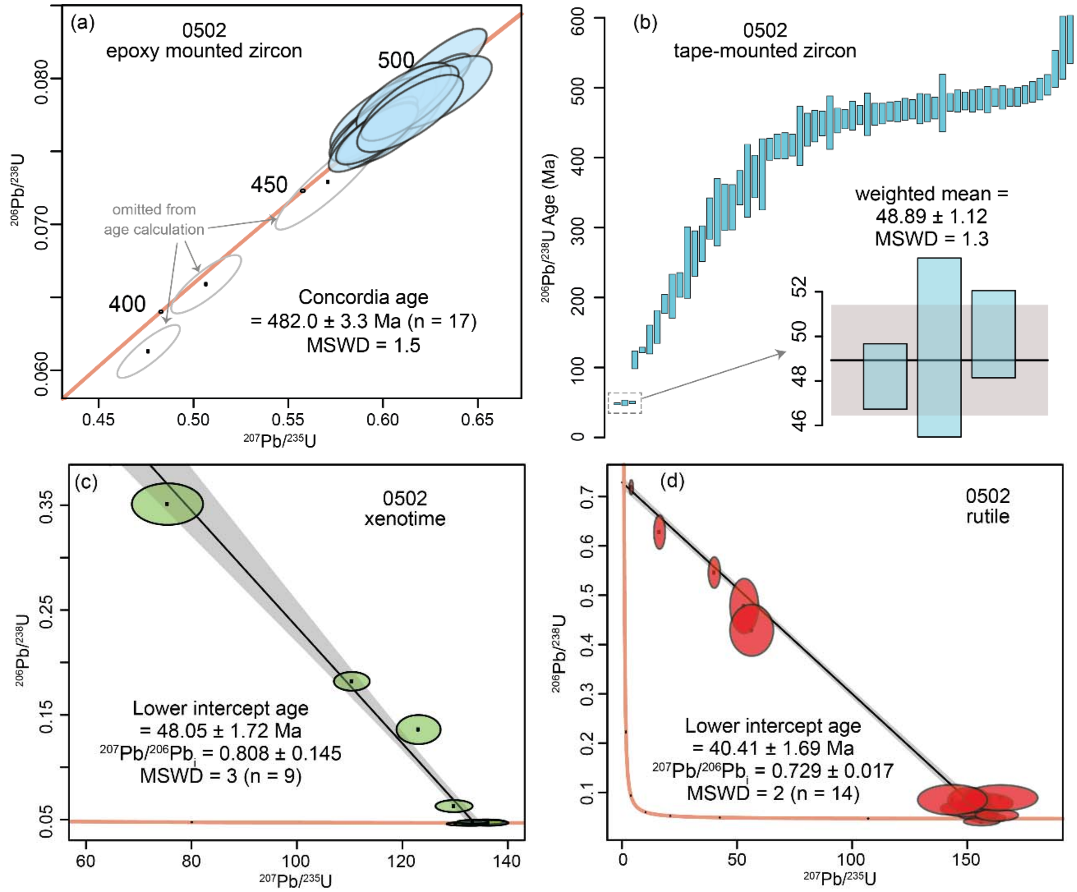

Fig. 6. A. U-Pb Wetherill plot showing U-Pb zircon core ages of Puga Gneiss sample 05-02. B. Rank-plot of all $_{206}$Pb/$_{238}$U zircon ages. An older age plateau represents the zircon cores at ~480 Ma. The youngest ages represent thin rims, and converge on a Himalayan age with a weighted average $_{206}$Pb/$_{238}$U age of the three youngest zircon ages. C. Tera-Wasserburg plot of xenotime U-Pb analyses. D. Tera-Wasserburg plot of rutile U-Pb analyses. Box heights and uncertainty ellipses are 2σ uncertainties.

3.2.2. Xenotime

Rare 30-100 µm xenotime grains were observed in micaceous aggregates at corroded margins of garnet in sample 05-02, as described above. The grains show homogenous brightness in BSE indicating the absence of internal zonation. Nine spots were analysed across 9 grains, and yield a mixing line between radiogenic and common lead components. Using a free regression, the lower intercept age is calculated at 48.05 ± 1.72 Ma (MSWD = 3; Figure 6c).

3.2.3. Rutile

Rutile grains in sample 05-02 measure 50-100 µm in size and show homogenous brightness in BSE, indicating the absence of internal zonation. Fourteen spots were analysed across 14 rutile grains, and yield a mixing line between radiogenic and common lead components. Using a free regression yields a lower intercept age of 40.41 ± 1.69 Ma (MSWD = 2; Figure 6d).

3.3. Retrogressed mafic eclogite (sample a03-12)

3.3.1. Zircon

Zircon grains are rarely found in mafic eclogites of the Tso Morari Complex. In thin section, zircons are often found as inclusions within eclogite-facies phases such as quartz and omphacite. Separated zircon grains from sample a03-12 are translucent and colourless with rounded and euhedral grain shapes and a grain size of < 70 μm (Figure 7f). They have zoning patterns dominated by broad oscillatory or sector zoning, that in some grains, truncates a darker core region; the latter were not analysed.

Thirteen laser spot analyses were performed on the cores of 13 zircon grains separated from sample a03-12 for U-Pb, with 3 analyses rejected due to Pb counts below detection. The U concentrations are variable (13.5-1528 ppm), as is the degree of the discordance ($^{207}Pb/^{206}Pb$ = 0.0479 – 0.1413). Of the remaining 10 analyses, the lower intercept of 9 spots is calculated using a free regression at 47.54 ± 0.81 Ma (MSWD = 0.63; Figure 7a). These zircon analyses have low Th/U ratios (<0.01). The result implies that the data conform to a single population. The omitted analyses has a much higher Th/U ratio (0.25), suggesting an igneous core region was clipped during the ablation.

Trace elements were measured on 20 zircon grains, including adjacent spots on the same 13 grains analysed for U-Pb; 3 analyses were omitted due to inclusions. Ti-in-zircon temperatures are calculated using Si and Ti activities of 1.0, and the equation of Ferry and Watson (2007). The temperatures range from 603 to 724 °C, forming a normal distribution around a peak at ca. 630 °C (Figure 7c). The REE data are plotted as chondrite-normalised values (Figure 7d). The REE patterns of zircon cores are broadly consistent across multiple grains, with no Eu anomaly, flat HREE patterns and depleted LREEs.

Several zircon grains were extracted from the resin mounts and prepared as single grain aliquots for CA-ID-TIMS. The resulting data are six reproducible fractions yielding a weighted mean (Th-corrected) $^{206}Pb/^{238}U$ age of 46.912 ± 0.036/0.046/0.068 Ma with an MSWD of 0.2 (Figure 7b).

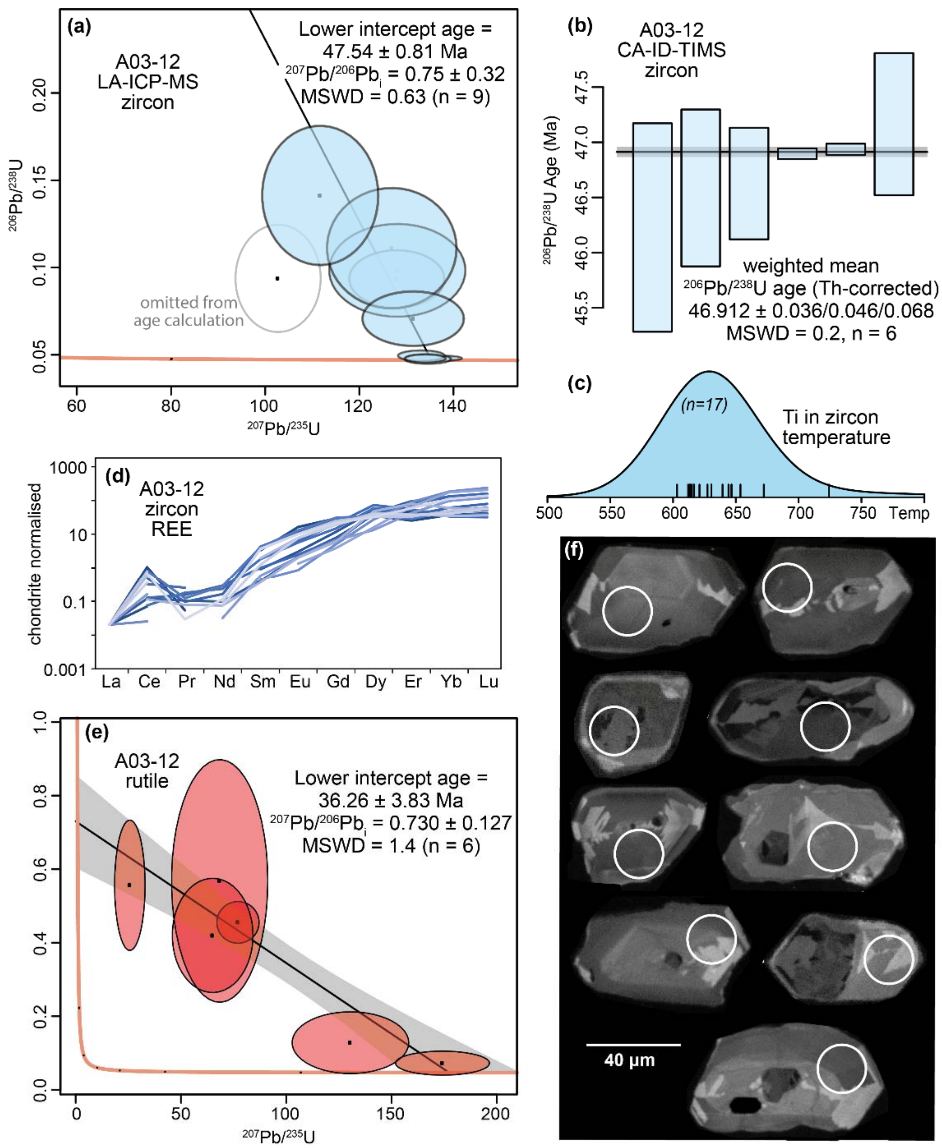

Figure 7. Mafic eclogite sample a03-12 a. Tera-Wasserburg plot of LA-ICP-MS U-Pb data for zircon, with lower intercept $^{206}Pb/^{238}U$ age and 1 sigma (%) error ellipses on data points. b. Weighted mean $^{206}Pb/^{238}U$ (Th corrected) age of 6 zircon grains using CA-ID-TIMS. C. Sample a03-12 zircon REE data. D. Tera-Wasserburg plot of LA-ICP-MS U-Pb data for rutile, with lower intercept $^{206}Pb/^{238}U$ age and 1 sigma (%) error ellipses on data points. e. Cathodoluminescence images of zircon separates from sample a03-12.

3.3.2. Rutile

Rutile grains in sample a03-12 show homogenous brightness in BSE with no indication of internal zonation. The majority of analyses had Pb counts below detection, the remaining data comprise six spots analysed across 6 grains. The analyses are distributed between the radiogenic and common lead components, and using a free regression, yield a lower intercept age of 36.26 ± 3.83 (MSWD = 1.4; Figure 7e).

3.4. Summary and Interpretations

3.4.1. Puga Gneiss (sample 05-02)

Zircon core ages of 482.0 ± 3.3 Ma in the Puga Gneiss are interpreted to represent the igneous crystallisation age and are comparable with U-Pb zircon ages of 479 ± 1 Ma in both the Polokongka La granite and the Puga Gneiss (Girard and Bussy, 1999). A monazite age of 473 ± 9 Ma in the Polokongka La granite, interpreted to have formed during crystallisation of the granite (Bidgood et al., 2022), also overlaps with the age of zircon crystallisation. Rim analyses of Ordovician zircon from the Puga Gneiss yielded an age of 48.89 ± 1.12 Ma (LA-ICP-MS), which overlap with high precision CA-ID-TIMS zircon age from mafic eclogite a03-12 (hosted within the gneiss), suggesting that zircon rims in the Puga gneiss also grew at eclogite-facies conditions.

Xenotime is found exclusively in Puga Gneiss sample 05-02, in mica aggregates adjacent to the corroded outer rim of a large garnet porphyroblast (Figures 2 and 3). Breakdown of parts of the Mg-enriched garnet rims, formed under peak eclogite-facies conditions (M2), liberated Y, which is concentrated in garnet zones P2 and P3 (Figure 3a), for xenotime growth. We therefore interpret the U-Pb xenotime age in sample 05-02 (48.1 ± 1.7 Ma) as the age of initial garnet breakdown during decompression. The xenotime age overlaps with the eclogite facies zircon rim age within the same sample 05-02 (48.89 ± 1.12 Ma), as well as the precise eclogite-facies zircon CA-ID-TIMS age of mafic eclogite sample a03-12 (46.91 ± 0.07 Ma), located within the same structural unit. This allows us to assign the xenotime crystallization and garnet breakdown in the Puga Gneiss sample to the M3a metamorphic assemblage, reflecting the earliest phase of decompression at eclogite facies conditions.

Rutile is present as inclusions within prograde (M1) to peak pressure (M2) garnets and the matrix of the Puga Gneiss. Given that the peak temperature of the Tso Morari Complex (705-755°C, St-Onge et al., 2013) is greater than the closure temperature of rutile, the U-Pb age of rutile can therefore be attributed to cooling of the Puga Gneiss through the rutile closure temperature at 40.4 ± 1.1 Ma, after peak temperature conditions.

3.4.2. Retrogressed mafic eclogite (sample a03-12)

LA-ICP-MS analyses of zircon from mafic eclogite sample a03-12 are entirely <50 Ma, and provide a weighted mean age of 47.5 ± 1.7 Ma. Although a limited dataset (9 analyses), our result implies a single population of metamorphic zircon, rather than preserving a protracted history of zircon growth. Flat HREE profiles and the lack of an Eu anomaly in the core and mantle of zircon grains are indicative of crystallisation in garnet-present, plagioclase-absent conditions, consistent with crystallisation in the eclogite facies (Schaltegger *et al.*, 1999; Rubatto, 2002; Rubatto and Hermann, 2003). The measured zircon date is therefore interpreted to correspond to growth within the eclogite-facies.

The zircon CA-ID-TIMS dates from mafic eclogite sample a03-12 are tightly clustered yielding a weighted mean $^{206}Pb/^{238}U$ (Th corrected) date of 46.91 ± 0.036/0.046/0.068 Ma n=6, MSWD=1.2 (uncertainties stated at analytical only/ analytical + tracer calibration for comparison with previous ID-TIMS U-Pb dates not using Earthtime Tracers/ Total uncertainty including ^{238}U decay constant)/Ma, which we interpret as the age of zircon growth at eclogite facies conditions (M1-3a). We note that this interpretation is heavily weighted to only the two analyses of most U-rich zircon, excluding these analyses yields a weighted mean of 46.71 ± 0.33/0.38/0.38 Ma (MSWD = 1.04; n=4) and is therefore within uncertainty of the favoured interpretation. Regardless of interpretation, the uncertainty associated with the CA-ID-TIMS data are 1 to 2 orders of magnitude greater than LA-ICPMS U-Pb data and provide the most precise estimate of the timing of metamorphic zircon growth from Tso Morari thus far. Additionally even with the improved precision the analyses and the lack of dispersion indicated by their MSWDs suggests no measurable crystal to crystal variation at around the ~1 Myr resolution.

Rutile is the peak titanium-bearing phase in mafic rocks during eclogite-facies metamorphism and is present as inclusions in garnet (M1), as well as in the matrix (M2-3b). Peak temperature in the Tso Morari Complex is estimated at 600-755°C (De Sigoyer et al., 2000; St-Onge et al., 2013), above the predicted closure temperature of rutile at ~630-400 °C (Cherniak, 2000; Li et al., 2013; Mezger et al., 1989; Vry & Baker, 2006) which is dependent on cooling rate and grain size (Zack and Koojiman, 2017; Oriolo et al., 2018). The U-Pb age of rutile can therefore be attributed to cooling through this closure temperature range.

4. Metamorphism, deformation and geochronology of the Tso Morari Complex

Previous studies indicate that subduction, exhumation and emplacement of the Tso Morari dome took place between c. 60 Ma and c. 7.5 Ma (Figure 6), with exhumation to lower crustal conditions by 45.3 ± 1.1 Ma at a rate of ~ 12 $mm.a^{-1}$ (St-Onge et al., 2013). The texture and composition of the mafic eclogites and Puga gneiss samples in this study collectively provide a record of initial exhumation from UHP eclogite-facies conditions, followed by exhumation through crustal conditions. Integrating this information with our new high-precision geochronology from a range of accessory phases which crystallized at different stages of metamorphism allows us to constrain the timing of mineral growth and fabric development with respect to the burial and exhumation of the Tso Morari.

Evidence of prograde metamorphism to peak pressures (M1-2) is preserved within garnets from mafic eclogite and the Puga Gneiss. Complex deformation fabrics and inclusion suites within a prograde garnet in the Puga Gneiss (Figure 3a,b) indicates that deformation and transformation of the original granite was already underway prior to garnet growth (M1) in the interior of the complex. This early fabric is rarely preserved in the Tso Morari Complex, where the earliest stage of deformation has been previously identified as the dominant top-to-the-east exhumation fabric within the Puga Gneiss and is attributed to initial M3a exhumation from eclogite-facies conditions (Epard and Steck, 2008).

Our eclogite-facies zircon dates of 46.91 ± 0.07 Ma (CA-ID-TIMS) and 47.5 ± 0.8 Ma (LA-ICPMS) from a mafic eclogite overlaps with our zircon rim and xenotime dates in the Puga Gneiss. We interpret this overlap as a record of the earliest phase of decompression at eclogite facies conditions, as recorded by the partial breakdown of yttrium-bearing garnet rims.

The formation of quartz microstructures during high-temperature (> 550°C) dynamic recrystallisation indicate that deformation took place during exhumation to crustal conditions (M3b). There is no significant overprinting of quartz deformation fabrics in the Puga Gneiss samples from the core of the dome suggesting that there was no pervasive deformation below 550°C. Deformation therefore occurred prior to cooling through the rutile closure temperature of ~630-400 °C (Cherniak, 2000; Li et al., 2013; Mezger et al., 1989; Vry & Baker, 2006) at 40.4 ± 1.1 Ma and was ductile and pervasive. Subsequent exhumation relating to doming and emplacement (M3c) was not pervasive, with foliations and lineations developing at the margins of the dome, adjacent to the normal sense shear zones (Epard and Steck, 2008; Bidgood *et al.*, 2020; Dutta and Mukherjee, 2021). The age of this is recorded in the Ar-Ar muscovite and biotite and apatite fission track dates of < 32.4 Ma (De Sigoyer et al., 2000; Schlup and Carter, 2003).

5. Discussion

5.1. Continental subduction and exhumation in the NW Himalaya

Our petrographic correlation of zircon and xenotime ages with the M3a assemblage indicates that zircon growth at ~ 47-46 Ma took place at subsolidus conditions during the earliest stages of decompression from UHP conditions. These ages overlap with the zircon age distribution peak of 47-43 Ma recorded by Donaldson et al. (2013). Considering their analytical scatter (i.e. MSWDs of 2.4 and 3.4) the Donaldson et al. dates have reasonable agreement with our 47-46 Ma age, however, those data were previously interpreted as a record of UHP metamorphism, *starting* at ~47 Ma. It is therefore necessary to reassess the Donaldson et al. (2013) data in light of our new data and observations, as follows.

Subsolidus zircon growth requires a fluid phase to mediate the liberation of zirconium from Zr-bearing phases (ilm, ru, cpx, grt) (Chen et al., 2010; Kohn et al., 2015; Chen and Zhang, 2017; Skuzovatov *et al.*, 2021). For Tso Morari, Palin et al. (2014) determined that the first pulse of post-peak fluid in the eclogite facies relates to the destabilisation of talc and growth of the coarse-grained amphiboles at ~23 kbar, followed by fluid infiltration from an external source at ~19 kbar. Coarse-grained, zoned amphiboles are abundant in mafic eclogites from across the Tso Morari Complex suggesting that post-peak eclogite facies hydration was a common and widespread occurrence, aided further by exhumation-related deformation. These influxes of fluid during exhumation, prior to a potentially dry spell at prograde to peak conditions, would have provided conditions favourable for high concentrations of zircon growth. Consequently, we argue that the breakdown of UHP garnet rims record by xenotime at 48.1 ± 1.7 Ma indicates that the zircon age peak at 47-43 Ma of Donaldson et al. (2013) reflects increased zircon growth during the onset of exhumation from UHP conditions, aided by the exhumation-driven liberation of fluids.

We suggest that the 58 ± 2.2 Ma zircon ages of St-Onge et al (2013) and the older zircon dates (53-48 Ma) from the Donaldson et al. (2013) dataset record zircon growth during prograde to peak metamorphism. More uncertain, are the nature of younger common-lead corrected dates from the Donaldson et al. dataset, especially considering that the authors found no relationship between the dates and the textural setting of the zircon (matrix grains versus inclusions in omphacite and garnet). Given that we consider our xenotime date as a marker for the onset of UHP exhumation, we suggest that the Donaldson et al. (2013) data do not reflect prograde to peak conditions after ca. 47 Ma.

Our new CA-ID-TIMS zircon age of 46.91 ± 0.046 Ma more closely and precisely correlates with ages from zircon (46.4 ± 0.1 Ma – ID-TIMS; 46.2 ± 0.7 – SHRIMP, 46 ± 2 Ma - SIMS) and allanite (46.5 ± 1.0 Ma – ID-TIMS) in UHP assemblages from Kaghan, located 450 km to the west (Kaneko et al., 2003; Parrish et al., 2006; Zhang et al., 2022) (see Figure 8). We do not think this is coincidental; metamorphic P-T data from both of these units record similar prograde and retrograde P-T paths. In Kaghan, coesite is found in thin metamorphic zircon rims in the felsic gneiss, suggesting that zircon crystallisation occurred at UHP conditions (Kaneko *et al.*, 2003). In the Tso Morari Complex, coesite is observed in the outermost rim of the prograde garnets but has not yet been observed as inclusions in zircon. Based on these similarities, we argue that the overlap in ages between Tso Morari and Kaghan indicates that UHP exhumation and associated fluid flux at 47-46 Ma was responsible for a ubiquitous pulse of zircon growth across the NW Himalaya. We suggest that the regional synchroneity between Tso Morari and Kaghan, across a distance of ~450 km, reflects the scale at which slab dynamics control metamorphism and exhumation with a subduction zone setting.

Lastly, cooling through the rutile closure temperature took place ~ 3.7 Ma later in Tso Morari than Kaghan (see Figure 8). At face value, this implies a longer period of time between zircon growth and exhumation through the rutile closure temperature for the Tso Morari Complex, relative to Kaghan. However, uncertainties in the exact conditions of zircon growth and rutile closure temperature prevents us from making any meaningful interpretation for the cause of this difference.

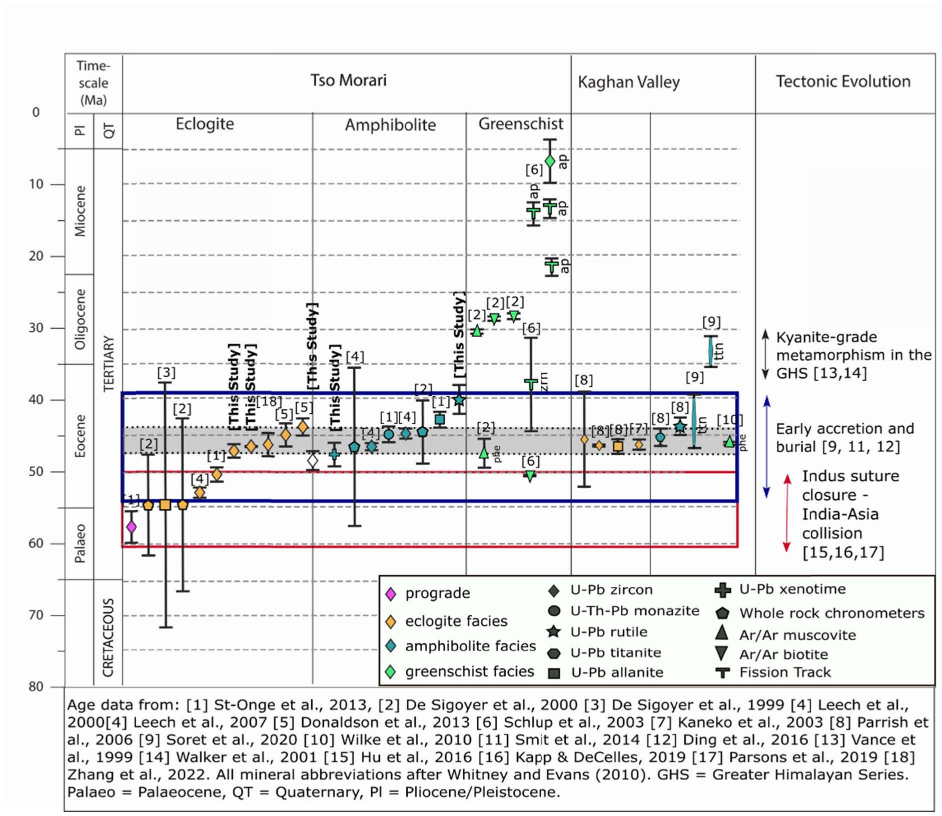

Figure 8: Time chart for Tso Morari and Kaghan, after (Palin *et al.*, 2012), comprising data from multiple sources, including this study.

5.2. UHP exhumation during the Himalayan orogeny

By associating accessory phase ages with distinct metamorphic assemblages, our data suggest that the episode of zircon crystallization recorded in the Tso Morari complex and Kaghan at 47-46 Ma, corresponds to the onset of exhumation of Indian continental crust from UHP conditions. In these following sections, we consider the significance of this event with respect to the wider metamorphic, magmatic and plate kinematic evolution of the Himalayan orogeny and the India-Australia-Eurasia plate network (Figure 9).

Within the NW Himalaya, the onset of UHP exhumation at 47-46 Ma overlaps with the onset of local prograde amphibolite facies, Barrovian-style metamorphism from 47 Ma to 39 Ma (Soret et al., 2021) (Figure 9a). Across the rest of the Himalaya, similar ages record accretion and crustal thickening via internal thrust stacking of the Himalayan metamorphic core (HMC) during 41-17 Ma (Ambrose et al., 2015, Carosi et al., 2016, Goscombe et al., 2018, Carosi et al., 2019, Mottram et al., 2019, Waters, 2019) with localized occurrences of high-pressure eclogite to granulite facies metamorphism of Indian lower crust recorded across the Himalaya from 40 Ma to 25 Ma (Figure 9a) (O'Brien, 2019, Chen et al., 2022).

In the upper plate of the orogen (Eurasian plate), significant magmatic and metamorphic changes also occurred during this time (Figure 9a). Between 50 Ma and 40 Ma, the isotopic signatures of magmatic rocks from the Kohistan-Ladakh batholith record crustal contamination between ~50 Ma and ~40 Ma (Bouilhol et al., 2013, Jagoutz et al., 2019). Along the Lhasa block, the Gangdese arc records adakite magmatism from ~48 Ma produced by melting of the Tibetan lower crust (e.g., Searle et al., 2011, Guan et al., 2012, Ma et al., 2014), and the cessation of subduction-related magmatism by ~40 Ma (e.g., Zhu et al., 2019). At the same time, the Lhasa block recorded high pressure-low temperature kyanite-grade partial melting associated with deformation and crustal thickening at 44-32 Ma (Zhang et al., 2010, Palin et al., 2014), whilst further to the east, the Mogok metamorphic belt and Eastern Ophiolite Belt in Myanmar record sillimanite-grade metamorphism between 48-22 Ma, which included a phase of granulite facies metamorphism between 43-32 Ma (Barley et al., 2003, Searle et al., 2007, Searle et al., 2017, Searle et al., 2020, Lamont et al., 2021).

From a plate-kinematic perspective (Figure 9c), UHP exhumation at 47-46 Ma coincides with a significant reorganisation of the India-Australia-Eurasia plate network (e.g., Patriat and Achache, 1984, Gibbons et al., 2015, Parsons et al., 2021). Between 45-40 Ma, the Indian plate underwent a 30%–38% reduction in plate speed (Molnar and Stock, 2009), which coincided with the onset of northward subduction of the Australian plate beneath southeast Asia and the coupling of the Indian and Australian plates (Figure 9c) (Smyth et al., 2008, Torsvik et al., 2008, Jacob et al., 2014, Gibbons et al., 2015, Parsons et al., 2021). Combined plate reconstruction and mantle tomographic analyses demonstrate that this plate network reorganisation occurred in response to collision of the Indian continent with the Eurasian margin at 50-40 Ma, and that continued convergence after that time was driven primarily by subduction of Australian oceanic lithosphere beneath southeast Asia to the east (Capitanio et al., 2015, Gibbons et al., 2015, Parsons et al., 2021, Bose et al., 2023).

The metamorphic and magmatic events recorded by the Himalayan orogeny between 50-40 Ma (Figure 9a) reflect a warming metamorphic thermal gradient and an increased mechanical coupling of the upper and lower plates, which are best explained by a reduction in the dip of the subducting Indian plate (e.g., Soret et al., 2021, Chen et al., 2022). Considering the plate kinematic restoration of the northern Indian continent margin and Eurasian margin which overlap during that time, we attribute this reduction in slab dip to the positive buoyancy of the Indian continental lithosphere within the collision zone, which stalled subduction and increased the component of under thrusting beneath Eurasia. We propose that UHP exhumation at 47-46 Ma occurred in response to this reduction in the vertical component of subduction, which allowed more time for thermally-assisted strain weakening mechanisms to detach slices of crustal material from the subducting slab, before it could be subducted to the point of no return (see discussion in Parsons et al., 2020). The mode of UHP exhumation is unclear, although isothermal, triclinic deformation during exhumation of the Tso Morari complex (Long et al., 2020; Dutta & Mukherjee, 2021) is most compatible with the recirculation and plunger models of Warren et al. (2008a, 2008b, 2008c). These models invoke the transport of crustal slices of the lower plate from UHP pressures along the subduction interface and can therefore occur independently from slab break-off.

In the context of double-collision models for the Himalayan orogeny, prograde to peak metamorphism of the Tso Morari complex between 60-50 Ma (Leech et al., 2007; St-Onge et al., 2013; Donaldson et al., 2013), as well as Barrovian metamorphism of the North Himalayan gneiss domes between 56-54 Ma (Smit et al., 2014, Ding et al., 2016), most likely corresponds to initial burial of the NW Himalaya during the first collision event (Figure 9a) which began at ~60 Ma (see introduction for definitions). In contrast, we argue that UHP exhumation at 47-46 Ma occurred during the second collision event (Figure 9a), corresponding to the collision of the Indian continent with Eurasia. Integrating our constraints for the timing of UHP exhumation with existing metamorphic, magmatic, and plate kinematic constraints (Figure 9a,c) suggests that the India-Asia collision, as defined by the second collision event, initiated between ~50-46 Ma.

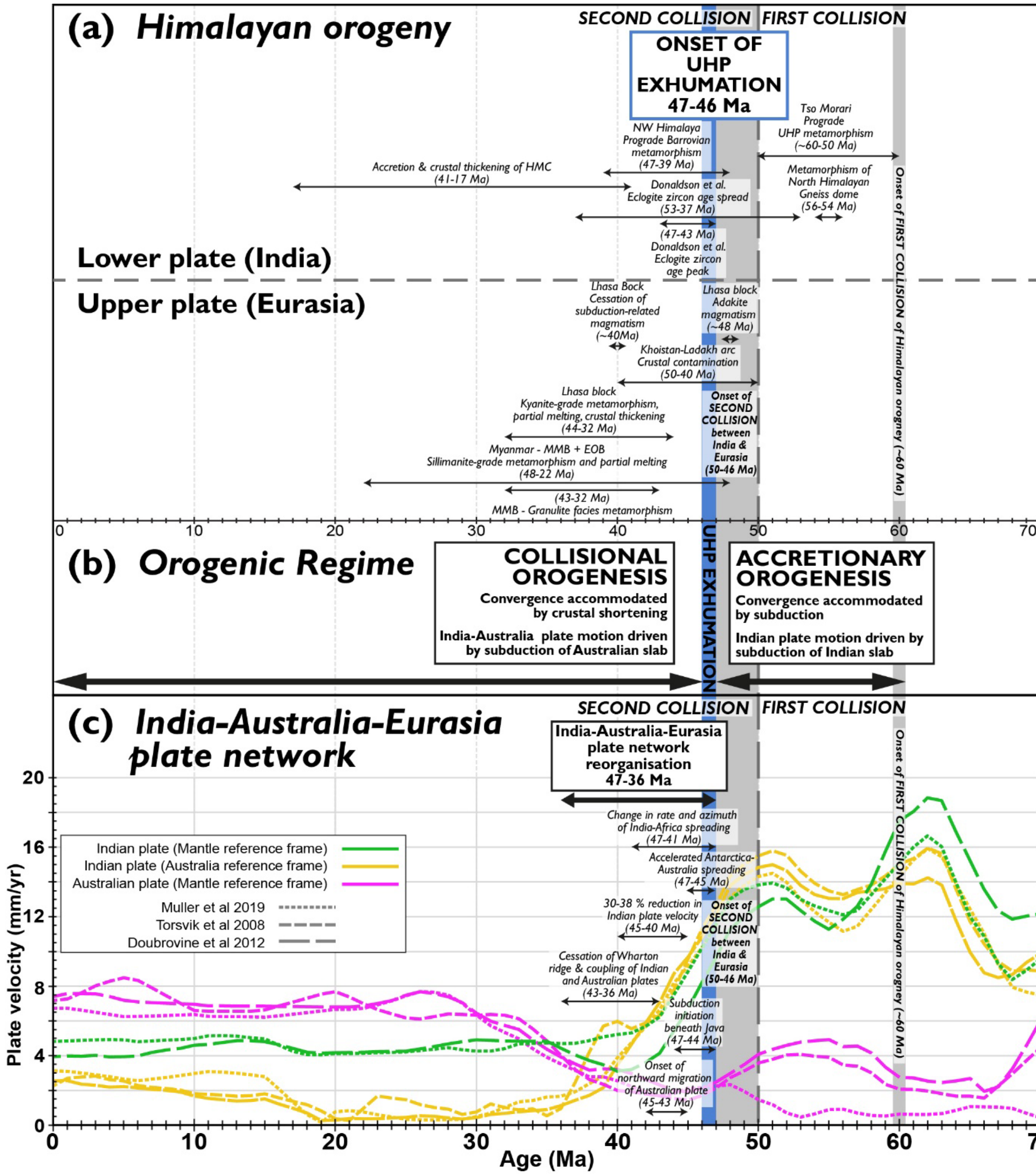

Figure 9. UHP exhumation at 47-46 Ma and its temporal relationship with the metamorphic, magmatic, and plate kinematic evolution of the Himalayan orogeny and India-Asutralia-Eurasia plate network. (a) Metamorphic and magmatic events in the Himlayan orogeny. (b) Orogenic regime of the Himalayan orogeny: onset of UHP exhumation marks the transition from an accretionary orogen to a collisional orogen (c.f., Cawood et al., 2009). (c) Reorganization of the India-Australia-Eurasia plate network at 47-36 Ma with plate velocity profiles for the Indian and Australian plates (Torsvik et al., 2008, Doubrovine et al., 2012, Müller et al., 2019). Data sources for events in (a) and (c) are cited in the main text. Significance for orogenesis and plate tectonics. (c) is modified after Parsons et al.

(2021). EOB – Eastern Ophiolite Belt; HMC – Himalayan Metamorphic core; MMB – Mogok Metamorphic Belt.

5.3. The significance of UHP exhumation for the geodynamics of orogenesis and plate tectonics

The occurrence of UHP exhumation at 47-46 Ma reflects a significant geodynamic shift of the Himalayan orogeny. Prior to this time, convergence between India and Asia and associated prograde high pressure-low temperature metamorphism of the NW Himalaya was accommodated by subduction of the Indian plate (Figure 9a). Then, following Second collision occurring by 47-46 Ma (see above), the buoyancy of the Indian continent switched the dominant mode of India-Asia convergence from subduction to crustal shortening. This switch in the mode of convergence, marked by the onset of UHP exhumation at 47-46 Ma, can be viewed as a shift in the geodynamic regime of the Himalaya (Figure 9b) from, (1) an *accretionary orogen*, in which convergence was driven and accommodated by subduction of a trailing Indian plate slab; to (2) a *collisional orogen*, in which convergence was accommodated by crustal shortening (*e.g.,* Replumaz et al., 2014; Cawood et al., 2009, Parsons et al., 2021, Chen et al., 2022). Collisional orogenesis since ~47-46 Ma, has been driven by subduction of Australian oceanic lithosphere beneath SE Asia, which also provided the driving force for India-Australia plate motion since that time (e.g., Li et al., 2008; Capitanio et al., 2015; Parsons et al., 2021, Bose et al., 2023).

At a broader perspective, whilst the occurrence of UHP exhumation reflects changes in local subduction dynamics and convergence mechanisms of the Himalayan orogeny (Figure 9b), those same changes also relate to the broader geodynamics and kinematics of the India-Eurasia-Australia plate network, as indicated by Figure 9c. The arrival of the buoyant Indian continent into the Eurasian subduction zone during second collision can be viewed as the trigger for (1) UHP exhumation, (2) the transition from accretionary orogenesis to collisional orogenesis (Figure 9b), and (3) the reorganisation of the India-Eurasia-Australia plate network (Figure 9c) (Patriat & Achache, 1984; Gibbons et al., 2015, Parsons et al., 2021), all starting at 47-46 Ma (Figure 9a). As such, the occurrence of UHP exhumation during orogenesis represents an important timestamp, marking a period of geodynamic and plate kinematic change, which can be dynamically linked to other tectonic events taking place at the same time, elsewhere in the same plate network (Figure 9).

6. Summary

By associating accessory phase ages with distinct metamorphic assemblages, and combining both high precision and high spatial resolution techniques, we demonstrate that the phase of peak zircon crystallization recorded in the Tso Morari complex at 46-47 Ma, corresponds to the onset of exhumation from UHP conditions. Zircon from a mafic eclogite have a U-Pb CA-ID-TIMS age of 46.91 ± 0.07 Ma (2σ) and an LA-ICPMS age of 47.5 ± 0.8 Ma, with REE profiles indicative of zircon crystallization at eclogite facies conditions. Those ages overlap with zircon rim ages (48.89 ± 1.1 Ma, LA-ICP-MS) and xenotime ages (48.1 ± 1.7 Ma; LA-ICP-MS) from the hosting Puga gneiss, which grew during breakdown of UHP garnet rims, as indicated by garnet element maps. Subsequent exhumation through the rutile closure temperature to crustal conditions is constrained by new dates of 40.4 ± 1.7 Ma and 36.3 ± 3.8 (2σ LA-ICP-MS).

The overlap between our mafic eclogite zircon ages, our xenotime-UHP garnet break down ages, indicate that the pulse of zircon growth recorded in the Tso Morari complex at 46-47 Ma (e.g., Donaldson et al., 2013) took place as a result of onset of exhumation from UHP conditions, rather than as a result of peak UHP metamorphism. These ages from Tso Morari overlap with U-Pb ID-TIMS, SHRIMP, and SIMS analyses of zircon from eclogite-facies mafic rocks in Kaghan and Naran, ~450-480 km to west of Tso Morari, which yielded ages of 46.4 ± 0.1 Ma, 46.2 ± 0.7 Ma, and 46 ± 2 Ma, respectively (Kaneko et al., 2003; Parrish et al., 2006; Zhang et al., 2022). We interpret this overlap as an indication that exhumation from UHP conditions occurred synchronously at 46-47 Ma across the whole of the NW Himalaya.

Integration of our new ages plus previously published ages from the NW Himalaya with existing metamorphic, magmatic, and plate kinematic constraints demonstrates that UHP exhumation at 47-46 Ma was triggered by the arrival of buoyant Indian continental lithosphere into the Eurasian subduction zone between 50-46 Ma. At a broader perspective, whilst the occurrence of UHP exhumation reflects changes in local subduction dynamics and convergence mechanisms of the Himalayan orogeny (Figure 9a-b), those same changes also relate to the broader geodynamics and kinematics of the India-Eurasia-Australia plate network (Figure 9c). Continent-continent collision of India and Asia at 50-46 Ma not only provided the trigger for UHP exhumation, but was also responsible for, (1) significant changes in the metamorphic and magmatic evolution of the Himalayan orogen (Figure 9a); (2) the transition of the Himalaya from an accretionary orogen to a collisional orogen (Figure 9b); and (3) a significant reorganisation of the wider India-Eurasia-Australia plate network (Figure 9c).

Our synthesis shows how the onset of UHP exhumation at 47-46 Ma temporally marks several changes in the geodynamic regime of the Himalayan orogen and the wider tectonic plate network, which stem from the onset of continent-continent collision. More generally, our study suggests that the occurrence of UHP exhumation during orogenesis can be viewed as an important timestamp marking a period of geodynamic and plate kinematic change and may be linked to other tectonic events taking place at the same time, elsewhere in the same orogen or further afield in the same plate network.

7. Supporting Information

7.1. Supporting Information 1. Geochronology of the northwest Himalaya

7.1.1. Table A1: Published geochronology results from Tso Morari and Kaghan.

7.2. Supporting Information 2. EPMA methods and data.

7.2.1. Methods

7.2.2. Table B1: EPMA data

7.3. Supporting Information 3: Geochronology data

7.3.1. Summary

7.3.2. ID-TIMS Zircon U-Pb

7.3.3. Laser Ablation Xenotime U-Pb

7.3.4. Laser Ablation Rutile U-Pb

7.3.5. Laser Ablation Zircon U-Pb

7.3.6. Laser Ablation Zircon trace elements

7.3.7. Run conditions Zircon

7.3.8. Run conditions Rutile

7.3.9. Run conditions trace elements

8. Acknowledgements

This work was funded by the Natural Environmental Research Council, grant number NE/L002612/1 awarded to AKB. Fieldwork to Ladakh was undertaken in 2016 and 2017 as part of the PhD of AKB and was partially funded by the Geological Society of London Mike Coward fund, the Mineralogical Society, Edinburgh Geological Society, University College Oxford and the Royal Geographical Society. Analytical work at the NERC Isotope Geosciences Laboratory was funded by NERC IP-1378-0507 and supported by CASE studentship number BUFI S330. For the purpose of Open Access, the author has applied a CC BY public copyright licence to any Author Accepted Manuscript version arising from this submission.

The EPMA, LA-ICPMS and ID-TIMS data used for geochemistry analysis and U-Pb dating in this study will be uploaded to the repository EarthChem with a DOI and an open access license prior to final submission of this manuscript. This data has also been submitted as supplementary information 2 and 3.

9. Figure captions

10. References

Ambrose, T.K., Larson, K.P., Guilmette, C., Cottle, J.M., Buckingham, H. & Rai, S. (2015). Lateral extrusion, underplating, and out-of-sequence thrusting within the Himalayan metamorphic core, Kanchenjunga, Nepal. Lithosphere, 7, 441-464. https://doi.org/10.1130/L437.1

An, W., Hu, X., Garzanti, E., Wang, J.-G. & Liu, Q. (2021). New Precise Dating of the India-Asia Collision in the Tibetan Himalaya at 61 Ma. Geophysical Research Letters, 48, e2020GL090641.

Babist, J., Handy, M. R., Konrad-Schmolke, M., & Hammerschmidt, K. (2006). Precollisional, multistage exhumation of subducted continental crust: The Sesia Zone, western Alps. Tectonics, 25(6). https://doi.org/10.1029/2005TC001927

Barley, M.E., Pickard, A.L., Zaw, K., Rak, P. & Doyle, M.G. (2003). Jurassic to Miocene magmatism and metamorphism in the Mogok metamorphic belt and the India-Eurasia collision in Myanmar. Tectonics, 22. https://doi.org/10.1029/2002TC001398

Beaumont, C., Jamieson, R. A., Butler, J. P., & Warren, C. J. (2009). Crustal structure: A key constraint on the mechanism of ultra-high-pressure rock exhumation. In Earth and Planetary Science Letters (Vol. 287, Issue 1). https://doi.org/10.1016/j.epsl.2009.08.001

Bidgood, A. K., Parsons, A. J., Lloyd, G. E., Waters, D. J., & Goddard, R. M. (2020). EBSD-based criteria for coesite-quartz transformation. Journal of Metamorphic Geology, 39(2), 165–180. https://doi.org/https://doi.org/10.1016/j.jsg.2018.06.012

Bidgood, A.K., Waters, D.J., Dyck, B.J. & Roberts, N.M.W. (2022). The emplacement, alteration, subduction and metamorphism of metagranites from the Tso Morari Complex, Ladakh Himalaya. Mineralogical Magazine, in press, https://doi.org/10.1180/mgm.2022.121

Bingen, B., Austrheim, H., & Whitehouse, M. (2001). Ilmenite as a source for zirconium during high-grade metamorphism? Textural evidence from the Caledonides of western Norway and implications for zircon geochronology. Journal of Petrology, 42(2), 355–375. https://doi.org/https://doi.org/10.1093/petrology/42.2.355

Bose, S., Schellart, W.P., Strak, V., Duarte, J.C. & Chen, Z. (2023). Sunda subduction drives ongoing India-Asia convergence. Tectonophysics, 849, 229727. https://doi.org/10.1016/j.tecto.2023.229727

Bouilhol, P., Jagoutz, O., Hanchar, J.M. & Dudas, F.O. (2013). Dating the India–Eurasia collision through arc magmatic records. Earth and Planetary Science Letters, 366, 163-175. https://doi.org/10.1016/j.epsl.2013.01.023

Boutelier, D., & Cruden, A. R. (2018). Exhumation of (U) HP/LT rocks caused by diachronous slab breakoff. Journal of Structural Geology, 117, 251–255. https://doi.org/https://doi.org/10.1016/j.jsg.2018.06.012

Brun, J.-P. & Faccenna, C. (2008). Exhumation of high-pressure rocks driven by slab rollback. Earth and Planetary Science Letters, 272, 1-7. https://doi.org/10.1016/j.epsl.2008.02.038

Buchs, N. and Epard, J.L., 2019. Geology of the eastern part of the Tso Morari nappe, the Nidar Ophiolite and the surrounding tectonic units (NW Himalaya, India). Journal of Maps, 15(2), pp.38-48. https://doi.org/10.1080/17445647.2018.1541196

Burg, J.-P. & Bouilhol, P. (2019). Timeline of the South Tibet – Himalayan belt: the geochronological record of subduction, collision, and underthrusting from zircon and monazite U–Pb ages. Canadian Journal of Earth Sciences, 56, 1318-1332. https://doi.org/10.1139/cjes-2018-0174

Burov, E., Francois, T., Agard, P., Le Pourhiet, L., Meyer, B., Tirel, C., Lebedev, S., Yamato, P. & Brun, J.-P. (2014). Rheological and geodynamic controls on the mechanisms of subduction and HP/UHP exhumation of crustal rocks during continental collision: Insights from numerical models. Tectonophysics, 631, 212-250. https://doi.org/10.1016/j.tecto.2014.04.033

Capitanio, F.A., Replumaz, A. & Riel, N. (2015). Reconciling subduction dynamics during Tethys closure with large-scale Asian tectonics: Insights from numerical modelling. Geochemistry, Geophysics, Geosystems, 16(3), pp.962-982. https://doi.org/10.1002/2014GC005660

Carosi, R., Montomoli, C., Iaccarino, S., Massonne, H.-J., Rubatto, D., Langone, A., Gemignani, L. & Visonà, D. (2016). Middle to late Eocene exhumation of the Greater Himalayan Sequence in the Central Himalayas: Progressive accretion from the Indian plate. GSA Bulletin, 128, 1571-1592. https://doi.org/10.1130/B31471.1

Carosi, R., Montomoli, C., Iaccarino, S. & Visonà, D. (2019). Structural evolution, metamorphism and melting in the Greater Himalayan Sequence in central-western Nepal. Geological Society, London, Special Publications, 483, 305-323. https://doi.org/10.1144/SP483.3

Cawood, P.A., Kröner, A., Collins, W.J., Kusky, T.M., Mooney, W.D. & Windley, B.F. (2009). Accretionary orogens through Earth history. Geological Society, London, Special Publications, 318, 1-36. https://doi.org/10.1144/SP318.1

Chatterjee, N., & Jagoutz, O. (2015). Exhumation of the UHP Tso Morari eclogite as a diapir rising through the mantle wedge. Contributions to Mineralogy and Petrology, 169(1), 3. http://doi.org/10.1007/s00410-014-1099-y

Chen, R. X., Zheng, Y. F., & Xie, L. (2010). Metamorphic growth and recrystallization of zircon: Distinction by simultaneous in-situ analyses of trace elements, U–Th–Pb and Lu–Hf isotopes in zircons from eclogite-facies rocks in the Sulu orogen. Lithos, 114(1–2), 132–154. https://doi.org/10.1016/J.LITHOS.2009.08.006

Chen, R.X. and Zheng, Y.F., (2017). Metamorphic zirconology of continental subduction zones. Journal of Asian Earth Sciences, 145, pp.149-176. https://doi.org/10.1016/j.jseaes.2017.04.029

Chen, S., Chen, Y., Guillot, S. & Li, Q. (2022). Change in Subduction Dip Angle of the Indian Continental Lithosphere Inferred From the Western Himalayan Eclogites. Frontiers in Earth Science, 9. https://doi.org/10.3389/feart.2021.790999

Cherniak, D. J. (2000). Pb diffusion in rutile. Contributions to Mineralogy and Petrology, 139(2), 198–207. https://doi.org/10.1007/PL00007671

Condon, D. J., Schoene, B., McLean, N. M., Bowring, S. A., & Parrish, R. R. (2015). Metrology and traceability of U–Pb isotope dilution geochronology (EARTHTIME Tracer Calibration Part I). Geochimica et Cosmochimica Acta, 164, 464–480. https://doi.org/10.1016/J.GCA.2015.05.026

Cottle, J. M., Jessup, M. J., Newell, D.L., Horstwood, M. S., Noble, S. R., Parrish, R. R., Waters, D. J., & Searle, M. P. (2009). Geochronology of granulitized eclogite from the Ama Drime Massif: Implications for the tectonic evolution of the South Tibetan Himalaya. Tectonics, 28(1). https://doi.org/https://doi.org/10.1029/2008TC002256

de Sigoyer, J;, Chavagnac, V., & Blichert-Toft, J. (2000). Dating the Indian continental subduction and collisional thickening in the northwest Himalaya: Multichronology of the Tso Morari eclogites. Geology, 28(6), 487–490. https://doi.org/https://doi.org/10.1130/0091-7613(2000)28<487:DTICSA>2.0.CO;2

de Sigoyer, J, & Guillot, S. (1997). Glaucophane-bearing eclogites in the Tso Morari dome (eastern Ladakh, NW Himalaya). European Journal of Mineralogy, 128(2–3), 197–212. https://doi.org/10.1127/ejm/9/5/1073

Degeling, H., & Eggins, S. (2001). Zr budgets for metamorphic reactions, and the formation of zircon from garnet breakdown. Mineralogical Magazine, 65(6), 749–758. https://doi.org/https://doi.org/10.1180/0026461016560006

Ding, H., Zhang, Z., Dong, X., Tian, Z., Xiang, H., Mu, H., Gou, Z., Shui, X., Li, W. & Mao, L. (2016). Early Eocene (c. 50 Ma) collision of the Indian and Asian continents: Constraints from the North Himalayan metamorphic rocks, southeastern Tibet. Earth and Planetary Science Letters, 435, 64-73. https://doi.org/10.1016/j.epsl.2015.12.006

Donaldson, D. G., Webb, A. A. G., Menold, C. A., Kylander-Clark, A. R. C., & Hacker, B. R. (2013). Petrochronology of Himalayan ultrahigh-pressure eclogite. Geology, 41(8), 835–838. https://doi.org/10.1130/G33699.1

Doubrovine, P.V., Steinberger, B. & Torsvik, T.H. (2012). Absolute plate motions in a reference frame defined by moving hot spots in the Pacific, Atlantic, and Indian oceans. Journal of Geophysical Research: Solid Earth, 117. https://doi.org/10.1029/2011JB009072

Dutta, D., & Mukherjee, S. (2021). Extrusion kinematics of UHP terrane in a collisional orogen: EBSD and microstructure-based approach from the Tso Morari Crystallines (Ladakh Himalaya). Tectonophysics, 800. https://doi.org/10.1016/j.tecto.2020.228641

Epard, J., & Steck, A. (2008). Structural development of the Tso Morari ultra-high pressure nappe of the Ladakh Himalaya. Tectonophysics, 451(1–4), 242–264. https://doi.org/https://doi.org/10.1016/j.tecto.2007.11.050

Foster, G. and Parrish, R.R., 2003. Metamorphic monazite and the generation of PTt paths. Geological Society, London, Special Publications, 220(1), pp.25-47. https://doi.org/10.1144/GSL.SP.2003.220.01.02

Fuchs, G., & Linner, M. (1996). On the geology of the suture zone and Tso Morari dome in Eastern Ladakh (Himalaya). Jahrbuch Der Geologischen Bundesanstalt, 139(191), 207.

Gansser, A., 1966. The Indian Ocean and the Himalayas, a geological interpretation: Eclogae Geol. Eclogae Geol. Helv. 67, 479–507.

Garzanti, E., & Van Haver, T. (1988). The indus clastics: forearc basin sedimentation in the Ladakh Himalaya (India). Sedimentary Geology, 59(3–4), 237–249. https://doi.org/10.1016/0037-0738(88)90078-4

Geisler, T., Schaltegger, U., & Tomaschek, F. (2007). Re-equilibration of Zircon in Aqueous Fluids and Melts. Elements, 3(1), 43–50. https://doi.org/10.2113/GSELEMENTS.3.1.43

Gibbons, A.D., Zahirovic, S., Müller, R.D., Whittaker, J.M. & Yatheesh, V. (2015). A tectonic model reconciling evidence for the collisions between India, Eurasia and intra-oceanic arcs of the central-eastern Tethys. Gondwana Research, 28, 451-492. https://doi.org/10.1016/j.gr.2015.01.001

Girard, M. (2001). Metamorphism and tectonics of the transition between non metamorphic Tethayan Himalaya sediments and the North Himalayan Crystalline Zone (Rupshuarea, Ladakh, NW India). Section Des Sciences de La Terre de l'université. http://www.unil.ch/files/live/sites/iste/files/shared/X.Library/Memoirs of Geology/35 – Girard (2001).pdf

Girard, M., & Bussy, F. (1999). Late Pan-African magmatism in the Himalaya: new geochronological and geochemical data from the Ordovician Tso Morari metagranites (Ladakh, NW India). Schweizerische Mineralogische Und Petrographische Mitteilungen, 79, 399–418. https://doi.org/http://doi.org/10.5169/seals-60215

Gordon, S., Little, T., Hacker, B., Bowring, S., Korchinski, M., Baldwin, S., & Kylander-Clark, A. (2012). Multi-stage exhumation of young UHP–HP rocks: Timescales of melt crystallization in the D'Entrecasteaux Islands, southeastern Papua New Guinea. Earth and Planetary Science Letters, 351, 237–246. https://doi.org/https://doi.org/10.1016/j.epsl.2012.07.014

Goscombe, B., Gray, D. & Foster, D.A. (2018). Metamorphic response to collision in the Central Himalayan Orogen. Gondwana Research, 57, 191-265. https://doi.org/10.1016/j.gr.2018.02.002

Guan, Q., Zhu, D.-C., Zhao, Z.-D., Dong, G.-C., Zhang, L.-L., Li, X.-W., Liu, M., Mo, X.-X., Liu, Y.-S. & Yuan, H.-L. (2012). Crustal thickening prior to 38Ma in southern Tibet: Evidence from lower crust-derived adakitic magmatism in the Gangdese Batholith. Gondwana Research, 21, 88-99. https://doi.org/10.1016/j.gr.2011.07.004

Guillot, S., Hattori, K., Agard, P., Schwartz, S. & Vidal, O. (2009). Exhumation Processes in Oceanic and Continental Subduction Contexts: A Review. Berlin, Heidelberg. Springer Berlin Heidelberg, 175-205. https://link.springer.com/chapter/10.1007/978-3-540-87974-9_10

Guillot, S., Mahéo, G., de Sigoyer, J., Hattori, K. H., & Pêcher, A. (2008). Tethyan and Indian subduction viewed from the Himalayan high- to ultrahigh-pressure metamorphic rocks. Tectonophysics, 451(1–4), 225–241. https://doi.org/10.1016/j.tecto.2007.11.059

Guillot, S., Sigoyer, J. De, & Lardeaux, J. (1997). Eclogitic metasediments from the Tso Morari area (Ladakh, Himalaya): Evidence for continental subduction during India-Asia convergence. Contributions to Mineralogy and Petrology, 128(2–3), 197–212. https://doi.org/10.1007/s004100050303

Green, O., Searle, M., Corfield, R., & Corfield, R. (2008). Cretaceous-Tertiary carbonate platform evolution and the age of the India-Asia collision along the Ladakh Himalaya (Northwest India). The Journal of Geology, 116(4), 331–353. http://www.jstor.org/stable/10.1086/588831

Hacker, B. R., & Gerya, T. V. (2013). Paradigms, new and old, for ultrahigh-pressure tectonism. Tectonophysics, 603, 79–88. https://doi.org/10.1016/j.tecto.2013.05.026

Hacker, B. R., Gerya, T. V., & Gilotti, J. a. (2013). Formation and exhumation of ultrahigh-pressure terranes. Elements, 9(4), 289–293. https://doi.org/10.2113/gselements.9.4.289

Hacker, B.R., Andersen, T.B., Johnston, S., Kylander-Clark, A.R.C., Peterman, E.M., Walsh, E.O. & Young, D. (2010). High-temperature deformation during continental-margin subduction & exhumation: The ultrahigh-pressure Western Gneiss Region of Norway. Tectonophysics, 480, 149-171. https://doi.org/10.1016/j.tecto.2009.08.012

Horstwood, M. S., Košler, J., Gehrels, G., Jackson, S. E., McLean, N. M., Paton, C., Pearson, N.J., Sircombe, K., Sylvester, P., Vermeesch, P., & Bowring, J. F. (2016). Community-derived standards for LA-ICP-MS U-(Th-) Pb geochronology–Uncertainty propagation, age interpretation and data reporting. Geostandards and Geoanalytical Research, 40(3), 311–332. https://doi.org/https://doi.org/10.1111/j.1751-908X.2016.00379.x

Hu, X., Garzanti, E., Wang, J., Huang, W., An, W. & Webb, A. (2016). The timing of India-Asia collision onset – Facts, theories, controversies. Earth-Science Reviews, 160, 264-299. https://doi.org/10.1016/j.earscirev.2016.07.014

Hu, X., Garzanti, E., Moore, T., & Raffi, I. (2015). Direct stratigraphic dating of India-Asia collision onset at the Selandian (middle Paleocene, 59±1 Ma). Geology,. Geology, 43(10), 859–862. https://doi.org/https://doi.org/10.1130/G36872.1

Ingalls, M., Rowley, D.B., Currie, B. & Colman, A.S. (2016). Large-scale subduction of continental crust implied by India–Asia mass-balance calculation. Nature Geoscience, 9, 848-853.

Jacob, J., Dyment, J. & Yatheesh, V. (2014). Revisiting the structure, age, and evolution of the Wharton Basin to better understand subduction under Indonesia. Journal of Geophysical Research: Solid Earth, 119, 169-190.

Jagoutz, O., Bouilhol, P., Schaltegger, U. & Müntener, O. (2019). The isotopic evolution of the Kohistan Ladakh arc from subduction initiation to continent arc collision. Geological Society, London, Special Publications, 483, 165-182. https://doi.org/10.1144/SP483.7

Jonnalagadda, M. K., Karmalkar, N. R., Duraiswami, R. A., Harshe, S., Gain, S., & Griffin, W. L. (2017). Formation of atoll garnets in the UHP eclogites of the Tso Morari Complex, Ladakh, Himalaya. Journal of Earth System Science, 126(8), 107. https://doi.org/10.1007/s12040-017-0887-y

Kaneko, Y., Katayama, I., Yamamoto, H., Misawa, K., Ishikawa, M., Rehman, H. U., Kausar, A. B., & Shiraishi, K. (2003). Timing of Himalayan ultrahigh-pressure metamorphism: sinking rate and subduction angle of the Indian continental crust beneath Asia. Journal of Metamorphic Geology, 21(6), 589–599. https://doi.org/10.1046/j.1525-1314.2003.00466.x

Kapp, P. & DeCelles, P.G. (2019). Mesozoic–Cenozoic geological evolution of the Himalayan-Tibetan orogen and working tectonic hypotheses. American Journal of Science, 319, 159-254. https://doi.org/10.2475/03.2019.01

Kohn, M.J., Engi, M. & Lanari, P. (2017). Petrochronology. Methods and Applications, Mineralogical Society of America Reviews in Mineralogy and Geochemistry, 83, 575.

Kohn, M. J., Corrie, S. L., & Markley, C. (2015). The fall and rise of metamorphic zircon. American Mineralogist, 100(4), 897–908. https://doi.org/10.2138/AM-2015-5064

Konrad-Schmolke, M., O'Brien, P., & Capitani, C. de. (2008). Garnet growth at high-and ultra-high pressure conditions and the effect of element fractionation on mineral modes and composition. Lithos, 103(3–4), 309–332. https://doi.org/https://doi.org/10.1016/j.lithos.2007.10.007

Kylander-Clark, A. R. C., Hacker, B. R., & Mattinson, J. M. (2008). Slow exhumation of UHP terranes: Titanite and rutile ages of the Western Gneiss Region, Norway. https://doi.org/10.1016/j.epsl.2008.05.019

Lamont, T.N., Searle, M.P., Hacker, B.R., Htun, K., Htun, K.M., Morley, C.K., Waters, D.J. & White, R.W. (2021). Late Eocene-Oligocene granulite facies garnet-sillimanite migmatites from the Mogok Metamorphic belt, Myanmar, and implications for timing of slip along the Sagaing Fault. Lithos, 386-387, 106027. https://doi.org/10.1016/j.lithos.2021.106027

Little, T.A., Hacker, B.R., Gordon, S.M., Baldwin, S.L., Fitzgerald, P.G., Ellis, S. & Korchinski, M. (2011). Diapiric exhumation of Earth's youngest (UHP) eclogites in the gneiss domes of the D'Entrecasteaux Islands, Papua New Guinea. Tectonophysics, 510, 39-68. https://doi.org/10.1016/j.tecto.2011.06.006

Long, S.P., Kohn, M.J., Kerswell, B.C., Starnes, J.K., Larson, K.P., Blackford, N.R. & Soignard, E. (2020). Thermometry and Microstructural Analysis Imply Protracted Extensional Exhumation of the Tso Morari UHP Nappe, Northwestern Himalaya: Implications for Models of UHP Exhumation. Tectonics, 39, e2020TC006482. https://doi.org/10.1029/2020TC006482

Lotout, C., Pitra, P., Poujol, M., Anczkiewicz, R. and Van Den Driessche, J., (2018). Timing and duration of Variscan high-pressure metamorphism in the French Massif Central: A multimethod geochronological study from the Najac Massif. Lithos, 308, pp.381-394. https://doi.org/10.1016/j.lithos.2018.03.022

Le Fort, P., 1975. Himalayas: the collided range. Present knowledge of the continental arc. Am. J. Sci. 275, 1–44.

Leech, M. L., Singh, S., & Jain, A. K. (2007). Continuous metamorphic zircon growth and interpretation of U-Pb SHRIMP dating: An example from the Western Himalaya. International Geology Review, 49(4), 313–328. https://doi.org/10.2747/0020-6814.49.4.313

Li, Q. L., Yang, Y. N., Shi, Y. H., & Lin, W. (2013). Eclogite rutile U–Pb dating: constraint for formation and evolution of continental collisional orogen. Chin Sci Bull, 58,. Chin Sci Bull, 58, 2279–2284.

Li, C., van der Hilst, R. D., Meltzer, A. S., & Engdahl, E. R. (2008). Subduction of the Indian lithosphere beneath the Tibetan Plateau and Burma. Earth and Planetary Science Letters, 274, 157–168. https://doi.org/10.1016/j.epsl.2008.07.016

Ma, L., Wang, B.-D., Jiang, Z.-Q., Wang, Q., Li, Z.-X., Wyman, D.A., Zhao, S.-R., Yang, J.-H., Gou, G.-N. & Guo, H.-F. (2014). Petrogenesis of the Early Eocene adakitic rocks in the Napuri area, southern Lhasa: Partial melting of thickened lower crust during slab break-off and implications for crustal thickening in southern Tibet. Lithos, 196-197, 321-338. https://doi.org/10.1016/j.lithos.2014.02.011

Mezger, K., Hanson, G., & SR Bohlen. (1989). High-precision UPb ages of metamorphic rutile: application to the cooling history of high-grade terranes. Earth and Planetary Science Letters, 96(1–2), 106–118. https://doi.org/https://doi.org/10.1016/0012-821X(89)90126-X

Molnar, P. & Stock, J.M. (2009). Slowing of India's convergence with Eurasia since 20 Ma and its implications for Tibetan mantle dynamics. Tectonics, 28. https://doi.org/10.1029/2008TC002271

Möller, C., Andersson, J., Dyck, B., & Antal Lundin, I. (2015). Exhumation of an eclogite terrane as a hot migmatitic nappe, Sveconorwegian orogen. Lithos, 226, 147–168. https://doi.org/10.1016/J.LITHOS.2014.12.013

Mottram, C.M., Cottle, J.M. & Kylander-Clark, A.R.C. (2019). Campaign-style U-Pb titanite petrochronology: Along-strike variations in timing of metamorphism in the Himalayan metamorphic core. Geoscience Frontiers, 10, 827-847. https://doi.org/10.1016/j.gsf.2018.09.007

Müller, R.D., Zahirovic, S., Williams, S.E., Cannon, J., Seton, M., Bower, D.J., Tetley, M.G., Heine, C., Le Breton, E., Liu, S., Russell, S.H.J., Yang, T., Leonard, J. & Gurnis, M. (2019). A Global Plate Model Including Lithospheric Deformation Along Major Rifts and Orogens Since the Triassic. Tectonics, 38, 1884-1907. https://doi.org/10.1029/2018TC005462

O'Brien, P.J., Zotov, N., Law, R.D., Khan, M.A., Jan, M.Q., et al. (2001). Coesite in Himalayan eclogite and implications for models of India-Asia collision. Geology 29(5): 435-438. https://doi.org/10.1130/0091-7613(2001)029<0435:CIHEAI>2.0.CO;2

O'Brien, P.J. (2019). Eclogites and other high-pressure rocks in the Himalaya: a review. Geological Society, London, Special Publications, 483, 183-213. https://doi.org/10.1144/SP483.13

O’Brien, P. J. (2006). The age of deep, steep continental subduction in the NW Himalaya: Relating zircon growth to metamorphic history. Comment on: “The onset of India–Asia continental collision: Early, steep subduction required by the timing of UHP metamorphism in the western . Earth and Planetary Science Letters, 245(3–4), 814–816. https://doi.org/10.1016/j.epsl.2006.03.033

O’Brien, P., & Sachan, H. (2000). Diffusion modelling in garnet from Tso Morari eclogite and implications for exhumation models. Earth Science Frontiers, 7, 25–27. http://d.wanfangdata.com.cn/periodical_dxqy2000z1010.aspx

Oriolo, S., Wemmer, K., Oyhantçabal, P., Fossen, H., Schulz, B. and Siegesmund, S., (2018). Geochronology of shear zones–A review. Earth-Science Reviews, 185, pp.665-683. https://doi.org/10.1016/j.earscirev.2018.07.007

Palin, R.M., Searle, M.P., St-Onge, M.R., Waters, D.J., Roberts, N.M.W., Horstwood, M.S.A., Parrish, R.R., Weller, O.M., Chen, S. & Yang, J. (2014). Monazite geochronology and petrology of kyanite- and sillimanite-grade migmatites from the northwestern flank of the eastern Himalayan syntaxis. Gondwana Research, 26, 323-347. https://doi.org/10.1016/j.gr.2013.06.022

Palin, R. M., St-Onge, M. R., Waters, D. J., Searle, M. P., & Dyck, B. (2014). Phase equilibria modelling of retrograde amphibole and clinozoisite in mafic eclogite from the Tso Morari massif, northwest India: constraining the P - T - M (H 2 O) conditions of exhumation. Journal of Metamorphic Geology, 32(7), 675–693. https://doi.org/10.1111/jmg.12085

Palin, R. M., Searle, M. P., Waters, D. J., Horstwood, M. S. A., & Parrish, R. R. (2012). Combined thermobarometry and geochronology of peraluminous metapelites from the Karakoram metamorphic complex, North Pakistan; New insight into the tectonothermal evolution of the

Baltoro and Hunza Valley regions. Journal of Metamorphic Geology, 30(8), 793–820. https://doi.org/https://doi.org/10.1111/j.1525-1314.2012.00999.x

Parrish, R., Gough, S., Searle, M., & Waters, D. (2006). Plate velocity exhumation of ultrahigh-pressure eclogites in the Pakistan Himalaya. Geology, 34(11), 989–992. https://doi.org/https://doi.org/10.1130/G22796A.1

Parsons, A.J., Hosseini, K., Palin, R.M. & Sigloch, K. (2020). Geological, geophysical and plate kinematic constraints for models of the India-Asia collision and the post-Triassic central Tethys oceans. Earth-Science Reviews, 208, 103084. https://doi.org/10.1016/j.earscirev.2020.103084

Parsons, A.J., Sigloch, K. & Hosseini, K. (2021). Australian Plate Subduction is Responsible for Northward Motion of the India-Asia Collision Zone and ∼1,000 km Lateral Migration of the Indian Slab. Geophysical Research Letters, 48, e2021GL094904. https://doi.org/10.1029/2021GL094904

Passchier, C. W., & Trouw, R. A. J. (2005). Deformation Mechanisms. In Microtectonics (pp. 25–66). Springer-Verlag. https://doi.org/10.1007/3-540-29359-0_3

Patriat, P. & Achache, J. (1984). India–Eurasia collision chronology has implications for crustal shortening and driving mechanism of plates. Nature, 311, 615-621. https://doi.org/10.1038/311615a0

Piazolo, S., Belousova, E., La Fontaine, A., Corcoran, C., & Cairney, J. M. (2017). Trace element homogeneity from micron- to atomic scale: Implication for the suitability of the zircon GJ-1 as a trace element reference material. Chemical Geology, 456, 10–18. https://doi.org/10.1016/J.CHEMGEO.2017.03.001

Puetz, S.J. & Spencer, C.J. (2023). Evaluating U-Pb accuracy and precision by comparing zircon ages from 12 standards using TIMS and LA-ICP-MS methods. Geosystems and Geoenvironment, 2, 100177.O’Brien, P. (2018). Tso Morari coesite eclogite: pseudosection predictions v. the preserved record and implications for tectonometamorphic models. Geological Society, London, Special Publications, 474(1), 5–24. https://doi.org/https://doi.org/10.1144/SP474.1

Regis, D., Warren, C.J., Mottram, C.M. and Roberts, N.M., (2016). Using monazite and zircon petrochronology to constrain the P–T–t evolution of the middle crust in the Bhutan Himalaya. Journal of Metamorphic Geology, 34(6), pp.617-639. https://doi.org/10.1111/jmg.12196

Replumaz, A., Capitanio, F.A., Guillot, S., Negredo, A.M., Villaseñor, A., 2014. The coupling of Indian subduction and Asian continental tectonics. Gondwana Res. 26, 608–626. https://doi.org/10.1016/j.gr.2014.04.003

Roberts, N. M., Thomas, R. J., & Jacobs, J. (2016). Geochronological constraints on the metamorphic sole of the Semail ophiolite in the United Arab Emirates. Geoscience Frontiers, 7(4), 609–619. https://doi.org/https://doi.org/10.1016/j.gsf.2015.12.003

Rubatto, D. (2002). Zircon trace element geochemistry: partitioning with garnet and the link between U–Pb ages and metamorphism. Chemical Geology, 184(1), 123–138. https://doi.org/10.1016/S0009-2541(01)00355-2

Rubatto, D., & Hermann, J. (2003). Zircon formation during fluid circulation in eclogites (Monviso, Western Alps): Implications for Zr and Hf budget in subduction zones. Geochimica et Cosmochimica Acta, 67(12), 2173–2187. https://doi.org/10.1016/S0016-7037(02)01321-2

Rubatto, D., Müntener, O., Barnhoorn, A., & Gregory, C. (2008). Dissolution-reprecipitation of zircon at low-temperature, high-pressure conditions (Lanzo Massif, Italy). American Mineralogist, 93(10), 1519–1529. https://doi.org/10.2138/AM.2008.2874

Sachan, H. K., Mukherjee, B. K., Ogasawara, Y., Maruyama, S., Ishida, H., Muko, A., & Yoshioka, N. (2004). Discovery of coesite from Indus Suture Zone (ISZ), Ladakh, India: Evidence for deep subduction. European Journal of Mineralogy, 16(2), 235–240. https://doi.org/10.1127/0935-1221/2004/0016-0235

Schaltegger, U., Fanning, C. M., Günther, D., Maurin, J. C., Schulmann, K., & Gebauer, D. (1999). Growth, annealing and recrystallization of zircon and preservation of monazite in high-grade metamorphism: Conventional and in-situ U-Pb isotope, cathodoluminescence and microchemical evidence. Contributions to Mineralogy and Petrology, 134(2–3), 186–201. https://doi.org/10.1007/s004100050478

Schlup, M., & Carter, A. (2003). Exhumation history of eastern Ladakh revealed by 40Ar/39Ar and fission-track ages: the Indus River–Tso Morari transect, NW Himalaya. Journal of the Geological Society, 3, 385–399. https://doi.org/https://doi.org/10.1144/0016-764902-084

Schwartz, S., Lardeaux, J. M., Tricart, P., Guillot, S., & Labrin, E. (2007). Diachronous exhumation of HP–LT metamorphic rocks from south-western Alps: evidence from fission-track analysis. Terra Nova, 19(2), 133–140. https://doi.org/10.1111/J.1365-3121.2006.00728.X

Searle, M.P., Noble, S.R., Cottle, J.M., Waters, D.J., Mitchell, A.H.G., Hlaing, T. & Horstwood, M.S.A. (2007). Tectonic evolution of the Mogok metamorphic belt, Burma (Myanmar) constrained by U-Th-Pb dating of metamorphic and magmatic rocks. Tectonics, 26. https://doi.org/10.1029/2006TC002083

Searle, M.P., Elliott, J.R., Phillips, R.J. & Chung, S.-L. (2011). Crustal–lithospheric structure and continental extrusion of Tibet. Journal of the Geological Society, 168, 633-672. https://doi.org/10.1144/0016-76492010-139

Searle, M.P., Morley, C.K., Waters, D.J., Gardiner, N.J., Htun, U.K., Nu, T.T. & Robb, L.J. (2017). Chapter 12 Tectonic and metamorphic evolution of the Mogok Metamorphic and Jade Mines belts and ophiolitic terranes of Burma (Myanmar). Geological Society, London, Memoirs, 48, 261-293. http://doi.org/10.1144/M48.12

Searle, M.P. (2019). Timing of subduction initiation, arc formation, ophiolite obduction and India–Asia collision in the Himalaya. Geological Society, London, Special Publications, 483, 19-37. https://doi.org/10.1144/SP483.8

Searle, M.P., Garber, J.M., Hacker, B.R., Htun, K., Gardiner, N.J., Waters, D.J. & Robb, L.J. (2020). Timing of Syenite-Charnockite Magmatism and Ruby and Sapphire Metamorphism in the Mogok Valley Region, Myanmar. Tectonics, 39, e2019TC005998. https://doi.org/10.1029/2019TC005998

Sinha Roy, S., 1976. A possible Himalayan microcontinent. Nature 263, 117–120. https://doi.org/10.1038/263117a0

Smit, M.A., Hacker, B.R. & Lee, J. (2014). Tibetan garnet records early Eocene initiation of thickening in the Himalaya. Geology, 42, 591-594. https://doi.org/10.1130/G35524.1

Smyth, H.R., Hall, R., Nichols, G.J., Draut, A.E., Clift, P.D. & Scholl, D.W. (2008). Cenozoic volcanic arc history of East Java, Indonesia: The stratigraphic record of eruptions on an active continental margin. Formation and Applications of the Sedimentary Record in Arc Collision Zones. Geological Society of America. 436, 0. https://doi.org/10.1130/2008.2436(10)

Soret, M., Larson, K.P., Cottle, J. & Ali, A. (2021). How Himalayan collision stems from subduction. Geology, 49, 894-898.Sheng, Y. M., Zheng, Y. F., Chen, R. X., Li, Q., & Dai, M. (2012). Fluid action on zircon growth and recrystallization during quartz veining within UHP eclogite: Insights from U–Pb ages, O–Hf isotopes and trace elements. Lithos, 136–139, 126–144. https://doi.org/10.1016/J.LITHOS.2011.06.012

Skuzovatov, S. Y., Shatsky, V. S., Ragozin, A. L., & Wang, K. L. (2021). Ubiquitous post-peak zircon in an eclogite from the Kumdy-Kol, Kokchetav UHP-HP Massif (Kazakhstan): Significance of exhumation-related zircon growth and modification in continental-subduction settings. Island Arc, 30(1), e12385. https://doi.org/10.1111/IAR.12385

St-Onge, M. R., Rayner, N., Palin, R. M., Searle, M. P., & Waters, D. J. (2013). Integrated pressure – temperature – time constraints for the Tso Morari dome (Northwest India): implications for the burial and exhumation path of UHP units in the western Himalaya. Journal of Metamorphic Geology, 31(5), 469–504. https://doi.org/10.1111/jmg.12030

Steck, A., Epard, J. L., Vannay, J. C., Hunziker, J., Girard, M., Morard, A., & Robyr, M. (1998). Geological transect across the Tso Morari and Spiti areas: The nappe structures of the Tethys Himalaya. Eclogae Geologicae Helvetiae, 91, 103–121. Stampfli, G.M., Borel, G.D., 2004. The TRANSMED transects in space and time: constraints on the paleotectonic evolution of the Mediterranean domain. In: Cavazza, W., Roure, F., Spakman, W., Stampfli, G.M., Ziegler, P.A. (Eds.), The TRANSMED Atlas. The Mediterranean Region from Crust to Mantle: Geological and Geophysical Framework of the Mediterranean and the Surrounding Areas. Springer, Berlin Heidel-berg, pp. 53–80. https://doi.org/10.1007/978-3-642-18919-7_3

Tapster, S., Condon, D. J., Naden, J., Noble, S. R., Petterson, M. G., Roberts, N. M. W., Saunders, A. D., & Smith, D. J. (2016). Rapid thermal rejuvenation of high-crystallinity magma linked to porphyry copper deposit formation; evidence from the Koloula Porphyry Prospect, Solomon Islands. Earth and Planetary Science Letters, 442, 206–217. https://doi.org/10.1016/J.EPSL.2016.02.046

Tomaschek, F., Kennedy, A. K., Villa, I. M., Lagos, M., & Ballhaus, C. (2003). Zircons from Syros, Cyclades, Greece—Recrystallization and Mobilization of Zircon During High-Pressure Metamorphism. Journal of Petrology, 44(11), 1977–2002. https://doi.org/10.1093/PETROLOGY/EGG067

Torsvik, T.H., Müller, R.D., Van der Voo, R., Steinberger, B. & Gaina, C. (2008). Global plate motion frames: Toward a unified model. Reviews of Geophysics, 46. https://doi.org/10.1029/2007RG000227

Tual, L., Smit, M.A., Kooijman, E., Kielman-Schmitt, M. and Ratschbacher, L., (2022). Garnet, zircon, and monazite age and REE signatures in (ultra) high-temperature and high-pressure rocks: Examples from the Caledonides and the Pamir. Journal of Metamorphic Geology, 40(8), pp.1321-1346. https://doi.org/10.1111/jmg.12667

van Hinsbergen, D.J.J., Lippert, P.C., Li, S., Huang, W., Advokaat, E.L. & Spakman, W. (2019). Reconstructing Greater India: Paleogeographic, kinematic, and geodynamic perspectives. Tectonophysics, 760, 69-94. https://doi.org/10.1016/j.tecto.2018.04.006

Vavra, G., Gebauer, D., Schmid, R., & Compston, W. (1996). Multiple zircon growth and recrystallization during polyphase Late Carboniferous to Triassic metamorphism in granulites of the Ivrea Zone (Southern Alps): an ion microprobe (SHRIMP) study. Contributions to Mineralogy and Petrology 1995 122:4, 122(4), 337–358. https://doi.org/10.1007/S004100050132

Vermeesch, P. (2018). IsoplotR: A free and open toolbox for geochronology. Geoscience Frontiers, 9(5), 1479–1493. https://doi.org/10.1016/J.GSF.2018.04.001

Vry, J., & Baker, J. (2006). LA-MC-ICPMS Pb–Pb dating of rutile from slowly cooled granulites: confirmation of the high closure temperature for Pb diffusion in rutile. Geochimica et Cosmochimica Acta, 70(7), 1807–1820. https://doi.org/https://doi.org/10.1016/j.gca.2005.12.006

Warren, C. J., Beaumont, C., Jamieson, R. A., & Lee, B. (2007). Detachment and Exhumation of Ultra-high-pressure Rocks During Continental Subduction. American Geophysical Union, Fall Meeting 2007, Abstract #V44A-01.

Warren, C J. (2013). Exhumation of (ultra-)high-pressure terranes: concepts and mechanisms. Solid Earth, 4, 75–92. https://doi.org/10.5194/se-4-75-2013

Warren, C. J., Beaumont, C., & Jamieson, R. A. (2008a). Formation and exhumation of ultra-high-pressure rocks during continental collision: Role of detachment in the subduction channel. Geochemistry, Geophysics, Geosystems, 9, Q04019. https://doi.org/10.1029/2007GC001839

Warren, C.J., Beaumont, C., & Jamieson, R. A. (2008b). Modelling tectonic styles and ultra-high pressure (UHP) rock exhumation during the transition from oceanic subduction to continental collision. In Earth and Planetary Science Letters, 267(1). https://doi.org/10.1016/j.epsl.2007.11.025

Warren, Clare J., Beaumont, C., & Jamieson, R. A. (2008c). Deep subduction and rapid exhumation: Role of crustal strength and strain weakening in continental subduction and ultrahigh-pressure rock exhumation. Tectonics, 27(6), n/a-n/a. https://doi.org/10.1029/2008TC002292

Waters, D.J. (2019). Metamorphic constraints on the tectonic evolution of the High Himalaya in Nepal: the art of the possible. Geological Society, London, Special Publications, 483, 325-375. https://doi.org/10.1144/SP483-2018-187

Weller, O. M., St-Onge, M. R., Rayner, N., Waters, D. J., Searle, M. P., & Palin, R. M. (2016). U–Pb zircon geochronology and phase equilibria modelling of a mafic eclogite from the Sumdo complex of south-east Tibet: Insights into prograde zircon growth and the assembly of the Tibetan plateau. Lithos, 262, 729–741. https://doi.org/10.1016/J.LITHOS.2016.06.005

Wilke, F., O'Brien, P., Gerdes, A., Tinnerman, M., Sudo, M., & Khan, M. (2010). The multistage exhumation history of the Kaghan Valley UHP series, NW Himalaya, Pakistan from U-Pb and 40Ar/39Ar ages. European Journal of Mineralogy, 22(5), 703–719. https://doi.org/https://doi.org/10.1127/0935-1221/2010/0022-2051

Wilke, F., O'Brien, P., Schmidt, A., & Ziemann, M. (2015). Subduction, peak and multi-stage exhumation metamorphism: Traces from one coesite-bearing eclogite, Tso Morari, western Himalaya. Lithos, 231, 77–91. https://doi.org/https://doi.org/10.1016/j.lithos.2015.06.007

Wu, Y. B., Zheng, Y. F., Zhao, Z. F., Gong, B., Liu, X., & Wu, F. Y. (2006). U–Pb, Hf and O isotope evidence for two episodes of fluid-assisted zircon growth in marble-hosted eclogites from the Dabie orogen. Geochimica et Cosmochimica Acta, 70(14), 3743–3761. https://doi.org/10.1016/J.GCA.2006.05.011

Xia, Q. X., Zheng, Y. F., Yuan, H., & Wu, F. Y. (2009). Contrasting Lu–Hf and U–Th–Pb isotope systematics between metamorphic growth and recrystallization of zircon from eclogite-facies metagranites in the Dabie orogen, China. Lithos, 112(3–4), 477–496. https://doi.org/10.1016/J.LITHOS.2009.04.015

Yamato, P., Burov, E., Agard, P., Le Pourhiet, L. & Jolivet, L. (2008). HP-UHP exhumation during slow continental subduction: Self-consistent thermodynamically and thermomechanically coupled model with application to the Western Alps. Earth and Planetary Science Letters, 271, 63-74. https://doi.org/10.1016/j.epsl.2008.03.049

Zack, T. and Kooijman, E., (2017). Petrology and geochronology of rutile. Reviews in Mineralogy and Geochemistry, 83(1), pp.443-467. https://doi.org/10.2138/rmg.2017.83.14

Zhang, D., Ding, L., Chen, Y., Schertl, H.-P., Qasim, M., Jadoon, U. K., et al. (2022). Two contrasting exhumation scenarios of deeply subducted continental crust in north Pakistan. Geochemistry, Geophysics, Geosystems, 23, e2021GC010193. https://doi.org/10.1029/2021GC010193

Zhang, Z.M., Zhao, G.C., Santosh, M., Wang, J.L., Dong, X. & Liou, J.G. (2010). Two stages of granulite facies metamorphism in the eastern Himalayan syntaxis, south Tibet: petrology, zircon geochronology and implications for the subduction of Neo-Tethys and the Indian continent beneath Asia. Journal of Metamorphic Geology, 28, 719-733. https://doi.org/10.1111/j.1525-1314.2010.00885.x

Zhou, J., Su, H., 2019. Site and timing of substantial India-Asia collision inferred from crustal volume budget. Tectonics 38, 2275–2290. https://doi.org/10.1029/2018TC005412

Zhu, D.-C., Wang, Q., Chung, S.-L., Cawood, P.A. & Zhao, Z.-D. (2019). Gangdese magmatism in southern Tibet and India–Asia convergence since 120 Ma. Geological Society, London, Special Publications, 483, 583-604. https://doi.org/10.1144/SP483.14